



CLICdp-Note-2019-005  
06 November 2019

## All-hadronic HZ production at high energy at 3 TeV CLIC

Emilia Leogrande<sup>a</sup>, Philipp Roloff<sup>a</sup>, Ulrike Schnoor<sup>a</sup>, Matthias Weber<sup>a,b</sup>

On behalf of the CLICdp Collaboration

<sup>a</sup> *CERN, Geneva, Switzerland*, <sup>b</sup> *University of Glasgow, United Kingdom*

### Abstract

In this note the HZ production in the all-hadronic final state in  $e^+e^-$  collisions at the Compact Linear Collider is studied at the 3 TeV stage. At high energies, the events have an experimental signature of back-to-back approximately mono-energetic large jets. Each of these jets contains two sub-jets and substructure compatible with two original objects. The study is based on full simulation including the detector response, as well as the presence of beam-induced background from  $\gamma\gamma \rightarrow$  hadrons. Results on the measurement of the total HZ cross section are given, and the potential to measure angular asymmetry observables is discussed.

*This work was carried out in the framework of the CLICdp Collaboration*

© 2019 CERN for the benefit of the CLICdp Collaboration.

Reproduction of this article or parts of it is allowed as specified in the CC-BY-4.0 license.

arXiv:1911.02523v1 [hep-ex] 6 Nov 2019

## 1. Introduction

The Compact Linear Collider (CLIC) is a mature option for a future electron-positron collider [1]. CLIC will be built in energy stages [2], achieving nominal centre-of-mass energies between 380 GeV and 3 TeV. A comprehensive discussion of the CLIC Higgs physics programme has been published in [3]. At the lowest energy stage of 380 GeV Higgsstrahlung ( $e^+e^- \rightarrow HZ$ ) is the dominant H boson production mechanism with a cross section of over 100 fb. The total cross section of the Higgsstrahlung can be measured in a model-independent way, i.e. without any additional assumption about the decays of the Higgs boson, using the quantities of the Z boson alone. This recoil method relies on precise knowledge of the  $\sqrt{s}$  of the collision and is only possible at lepton colliders.

At high energy, the cross section for the Higgsstrahlung process decreases as  $1/s$ , where  $\sqrt{s}$  is the centre-of-mass energy, and W W-fusion ( $e^+e^- \rightarrow H\nu_e\bar{\nu}_e$ ) dominates the H production. However, contributions from some Standard Model Effective Field Theory (EFT) operators grow with energy. Measurements of the Higgsstrahlung production rate at the higher CLIC energy stages enhance the sensitivity to New Physics as illustrated in [4]. Recent EFT analyses of Higgs and electroweak processes including projections for Higgsstrahlung at the high energy CLIC stages are described in [5, 6]. We present a study of the process  $e^+e^- \rightarrow ZH \rightarrow$  with  $Z \rightarrow q\bar{q}$  and  $H \rightarrow b\bar{b}$  at the 3 TeV CLIC stage based on full detector simulation. This fully hadronic final state is expected to provide the best statistical precision.

Additional sensitivity on EFT operators is provided by angular observables [7]. Projections from a generator-level study using leptonic Z boson decays are shown in chapter 2.3 of [8]. The potential of events with hadronic Z decays based on full detector simulation is described here.

Due to the high energy, two large jets are reconstructed and ZH signal events are identified using substructure information. B-tagging in boosted H boson decays at CLIC is investigated for the first time for the analysis presented here. Different methods for the charge reconstruction in subjects are compared

The study uses the updated luminosity numbers and the baseline scenario for luminosity sharing of  $L_{-80\%} = 4 \text{ ab}^{-1}$  and  $L_{+80\%} = 1 \text{ ab}^{-1}$  for -80% and +80% polarisation of the electron beam [9].

This paper is organized as follows: Section 2 describes the CLIC detector model, and the software packages in use, while section 3 gives an overview of the overall HZ topology and signal reconstruction. Section 4 contains considerations for B-tagging in boosted jet topologies. Section 5 describes the Monte Carlo Simulation. The details about the background rejection and signal selection are discussed in section 6. Section 7 presents the cross section and results on the angular distributions, followed by a discussion of systematic uncertainties in section 8. Section 9 concludes with a summary.

## 2. Detector model and software chain

This study is based on the new detector model CLICdet, which was developed in several optimisation studies [10, 11]. The CLICdet model is designed to cope with experimental conditions at 3 TeV CLIC. The central feature of CLICdet is a superconducting solenoid with an internal diameter of 7 m, providing a magnetic field of 4 T in the centre of the detector. Silicon pixel and strip trackers, the electromagnetic (ECAL) and hadronic calorimeters (HCAL) are embedded within the solenoid. Each subdetector is divided into a barrel and two endcap sections. ECAL is a highly granular array of 40 layers of silicon sensors and tungsten plates. HCAL is built from 60 layers of plastic scintillator tiles, read out by silicon photomultipliers, and steel absorber plates. The muon system surrounding the solenoid consists in the endcap of 6, in the barrel of 7 layers of resistive plate chambers interleaved with yoke steel plates. Two smaller electromagnetic calorimeters, LumiCal and BeamCal, cover the very forward region of CLICdet on either side of the interaction point.

CLICdet uses a right-handed coordinate system, with the origin at the nominal point of interaction. The z-axis is along the beam direction, with the electron pointing in the positive direction. The y-axis points upwards along the vertical direction. The crossing angle between the electron and positron beams

is 20 mrad, with electron momentum  $p_x^- > 0$  and positron momentum  $p_x^+ > 0$ . The polar angle  $\theta$  is measured from the positive  $z$ -axis.

A new software chain for simulation and reconstruction has been introduced, using the DD4hep detector description toolkit [12, 13]. The detector response is simulated using the GEANT4 10.02.p02 toolkit [14]. Beam-induced backgrounds from  $\gamma\gamma \rightarrow$  hadrons are simulated using the GUINEAPIG program [15] and CLIC beam parameters at 3 TeV. These background collisions are overlaid on the hard physics event. Tracks are reconstructed using the conformal tracking pattern recognition technique [16]. Software compensation is applied to hits in HCAL to improve the energy measurement, using local energy density information [17]. Pandora particle flow algorithms [18, 19] combine information from tracks, calorimeter clusters and muon hits for particle identification and reconstruction. Jet clustering, jet substructure variables, and the jet resolution parameters ( $y_{23}, y_{34}$ ) are calculated using the FastJet 3.3.2 [20] library. The performance of track reconstruction, particle identification, and flavour tagging at CLICdet has been studied with the new software chain in [11]. Relative jet energy resolution values at 3 TeV CLIC are typically around 6–8% for jet energies around 50 GeV, decreasing to 4.5–6% for jet energies larger than 100 GeV, and about 3–4% for 1 TeV jets. In this paper, the relevant jet energies are above 1 TeV.

### 3. HZ event and signal reconstruction

At very high energy the quarks from the Z boson are produced very close to each other, as are the decay products of the H boson. Thus all-hadronic HZ events are characterised by two back-to-back “fat” jets, each containing two very close-by subjets. Jets are reconstructed with the VLC algorithm [21] as implemented in the FastJet library [20] with a radius  $R = 0.7$  and  $\gamma = \beta = 1$  in exclusive mode to force the event into two jets. The VLC algorithm combines a Durham like inter-particle distance  $d_{ij} = 2 \min(E_i^{2\beta}, E_j^{2\beta})(1 - \cos \theta_{ij})/R^2$  based on energy and polar angle with a beam distance  $d_{iB} = E_i^{2\beta} \sin^{2\gamma} \theta_{iB}$ . The algorithm applies a sequential recombination procedure, providing a robust performance at  $e^+e^-$  colliders with non-negligible background. The jet algorithm clusters particle flow objects, identified by the Pandora particle flow algorithms [18, 19]. Prior to jet clustering  $p_T$  and tight timing cuts are applied to the particle flow objects, to reject hadrons originating from  $\gamma\gamma \rightarrow$  hadrons. The timing requirements and the impact of timing cuts at CLIC are described in detail in the CDR [22, Section 2.5]. The radius of  $R = 0.7$  is sufficient to catch the energy of both partons in one jet. At energies of around 1 TeV and larger, the relative jet energy resolution is between 3% to 4% for almost all polar angles. The dominating Higgs boson decay mode in the Standard Model is  $H \rightarrow b\bar{b}$  with around 58.4%, at a mass of  $m_H = 125$  GeV. Thus the event selection is based on finding events with two high-energy back-to-back jets, each containing two subjets. Each one of the jets are required to have jet masses compatible with Z or H. Concentrating on the most dominant decay channel and in order to suppress backgrounds, the jet compatible with H needs to be B-tagged.

Reconstructed jets are spatially matched to the Z and H parton directions to evaluate their mass resolution. As Figure 1 shows, both jet mass distributions peak close to the Z and H masses. While the Z jet mass distribution is symmetric, for the H jet the mass distribution is asymmetric and significantly shifted to lower values. The H jet decays predominantly into b-quarks, and a sizeable fraction of B mesons and baryon decays involves neutrinos, which escape detection. Since genuine missing energy is not present in the hard process of all-hadronic decays of HZ, this bias can be partially recovered, using the reconstructed missing transverse momentum. The missing transverse momentum vector is projected onto the transverse momentum vector of the jet, which is in the same hemisphere as the missing transverse momentum  $\vec{p}_T^{\text{miss}}$ . The projected missing transverse momentum  $\vec{p}_T^{\text{miss,proj}}$  is added on top of the jet transverse momentum, thus  $\vec{p}_T' = \vec{p}_T + \vec{p}_T^{\text{miss,proj}} = f \cdot \vec{p}_T$  with  $f > 1$ . The jet is very boosted and most particles are aligned with the jet axis. Thus the  $z$ -momentum of the jet is scaled with the same scale-factor and

$\vec{p}' = f \cdot p$ . Since neutrino masses are negligible to the scale of the neutrino momentum, the energy is modified to  $E' = E + (f - 1) \cdot p$ , where  $p$  is the original total momentum of the jet. This correction procedure improves the mass resolution of the reconstructed jet matched to the H boson significantly: the distribution is now symmetric, and the mean of the distribution moves closer to the H mass as shown in Fig. 1. Besides improving the mass reconstruction, the correction improves both the momentum (see Fig. 2) and the energy of the reconstructed jets (see Fig. 3) separately as well. After applying the missing transverse momentum correction, the leading reconstructed jet in terms of jet mass, referred to as *jet1*, is assigned as H and the second leading jet is assigned as Z, referred to as *jet2* in the following. This procedure leads to the correct assignment of jets to the bosons in 85% of events for high- $\sqrt{s}$  events. After a final signal selection, the selection by mass is accurate to about 98%.

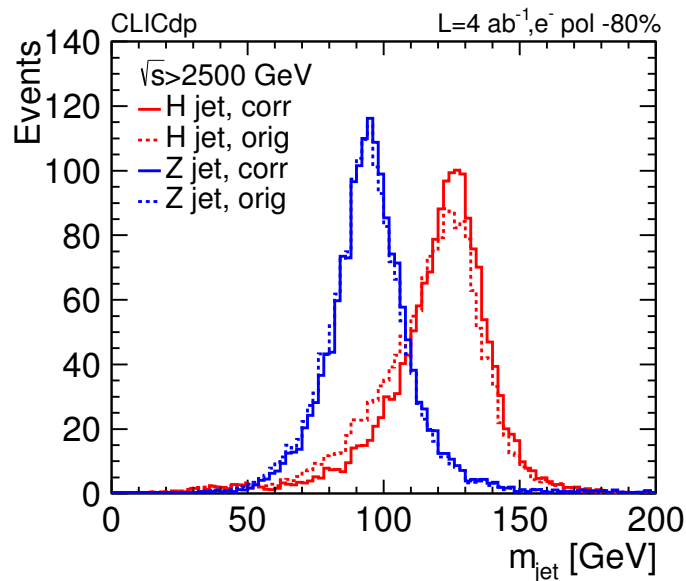


Figure 1: The mass distributions of jets, matched to the H and Z parton direction, for boosted events with  $H \rightarrow b\bar{b}$  and reconstructed  $\sqrt{s} > 2500\text{ GeV}$  after correcting the jets. The solid lines are the distributions after correcting the jet with the missing transverse momentum vector, the dashed lines represent the reconstructed masses before the correction is applied.

This study focuses on high energy  $\sqrt{s}$  events. The  $\sqrt{s}$  spectrum of all HZ events on parton level is shown in Fig. 4. It combines the effects of the luminosity spectrum, which peaks at 3 TeV with the steeply falling cross section for HZ as function of  $\sqrt{s}$ . In this note the interest is on the high-energy part of the  $\sqrt{s}$  spectrum.

On reconstructed level four different methods are investigated to determine  $\sqrt{s}$ . The first method uses the four-momentum vector sum of all reconstructed particle flow objects after subtracting isolated photons under the assumption that these originate from beam radiation. The second method corrects this sum by the missing transverse momentum correction vector. The third method uses the four-momentum vector sum of the reconstructed jets to derive  $\sqrt{s}$ . The fourth method uses the four-momentum vector sum of the reconstructed jets after applying the transverse momentum projection correction. The performance of the four methods is shown in Fig. 5 comparing the ratio of the reconstructed  $\sqrt{s}$  and the real partonic  $\sqrt{s}$  for  $\sqrt{s} > 2500\text{ GeV}$ . The fourth method – using jets after the transverse momentum projection correction – performs best, the mean is closest to zero and the width of the distribution is the smallest. Thus this method is used in the following. The first and second method suffer from the impact of beam-induced background events from  $\gamma\gamma \rightarrow \text{hadrons}$ . These hadrons tend to be forward and increase the recorded event energy by order of 100 GeV. The jet properties are only mildly affected by these

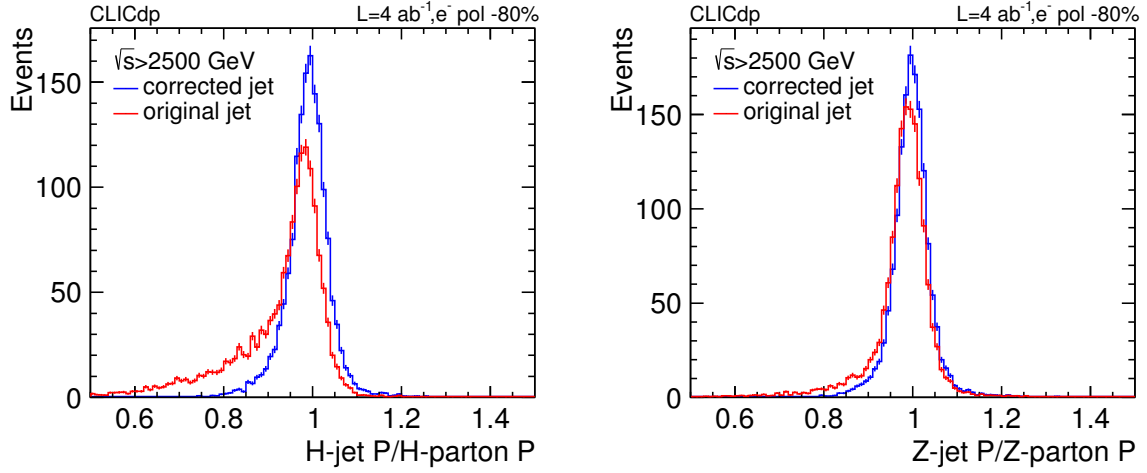


Figure 2: Impact of the missing transverse momentum correction procedure on the jet momentum for jets matched to the partonic H (left) and Z (right) bosons for boosted events with  $H \rightarrow b\bar{b}$  and reconstructed  $\sqrt{s} > 2500\text{ GeV}$  after correcting the jets.

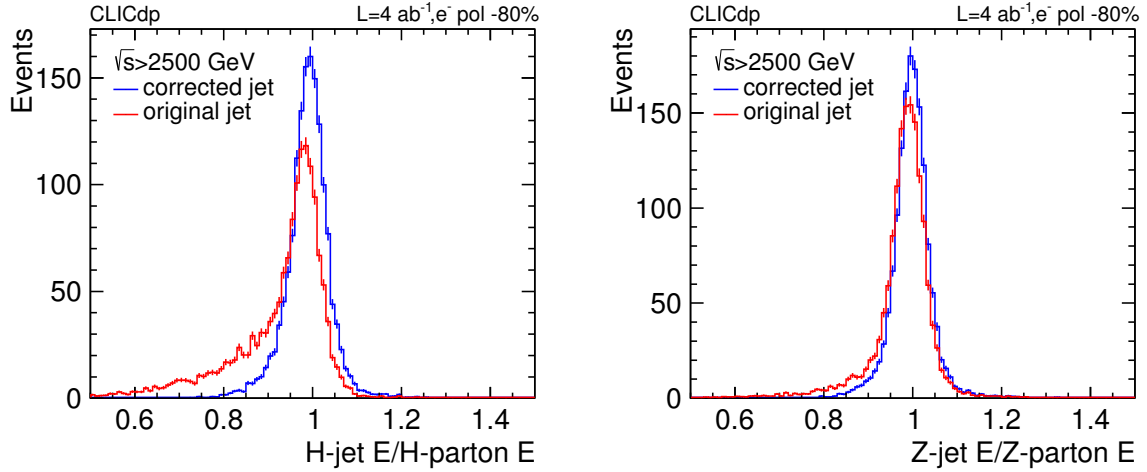


Figure 3: Impact of the missing transverse momentum correction procedure on the jet energy for jets matched to the partonic H (left) and Z (right) bosons for boosted events with  $H \rightarrow b\bar{b}$  and reconstructed  $\sqrt{s} > 2500\text{ GeV}$  after correcting the jets.

hadrons [11]. Due to the large boost at high energies, the unclustered energy outside of the jet cone is negligible.

The final goal is the measurement of angular asymmetries, which have been found to be particularly sensitive to subtle effects which can point towards an extension of the SM. The asymmetries  $A_{c\theta_1, c\theta_2}$ ,  $A_{\theta_1}$ ,  $A_{\phi}^{(1)}$ ,  $A_{\phi}^{(2)}$ ,  $A_{\phi}^{(3)}$ , and  $A_{\phi}^{(4)}$  are defined in terms of three angles [23]. The angle  $\theta_1$  is defined as the angle between the positively charged fermion  $f^+$  of the Z boson decay in the Z centre-of-mass-system and the flight direction of the Z boson. The angle  $\theta_2$  is defined as the angle between the H boson and the incoming  $e^+$  direction in the HZ centre-of-mass-system. The third angle  $\phi$  is defined as the angle between the H- $e^+$  and  $f^+$ -Z planes. Previous studies concentrated on HZ events with leptonic Z-decays  $Z \rightarrow l^+l^-$  [23, 24] (with  $l = e, \mu$ ) where backgrounds are small, and the positively charged lepton can be identified with high accuracy. In this note the possibility to measure HZ in an all-hadronic signature is

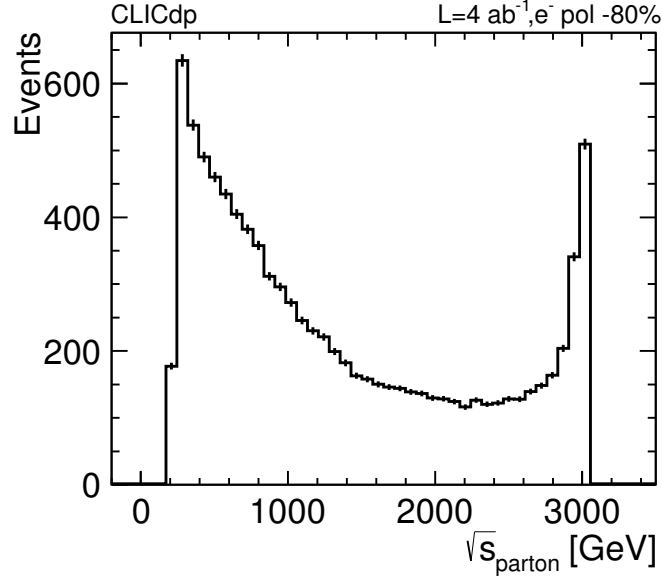
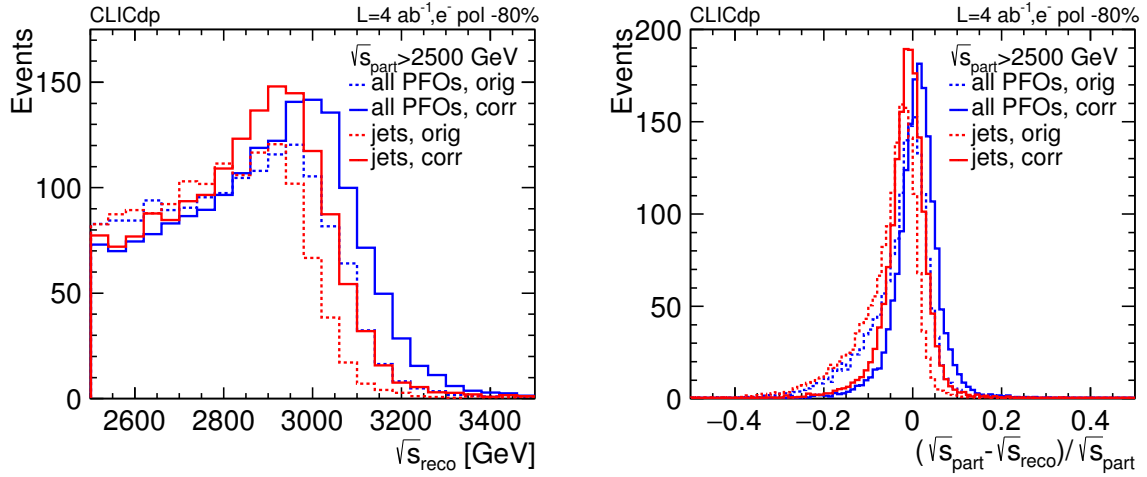
Figure 4: The parton level centre-of-mass energy  $\sqrt{s}$ .

Figure 5: Comparison of four methods to reconstruct the centre-of-mass energy  $\sqrt{s}$ : the reconstructed distributions at high-energy are shown on the left, the relative ratio with respect to the partonic  $\sqrt{s}$  are shown on the right. Events with  $H \rightarrow b\bar{b}$  and partonic  $\sqrt{s}_{\text{part}} > 2500 \text{ GeV}$  are considered.

investigated. This branching ratio is about a factor of ten larger than Z decays into muons or electrons. Following the strategy for HZ with  $Z \rightarrow l^+l^-$  for events with  $Z \rightarrow q\bar{q}$  the positively charged quark of the Z boson decay has to be identified. The two sub-jets of the second jet are identified using FastJet in the exclusive subjet clustering mode. This effectively undoes the last clustering step of the VLC jet clustering of the second jet. Both the direction and energy sharing between both sub-jets replicate the energy ratios and the direction of the quarks on parton level satisfactory. The sub-jet charge  $Q_{sj}$  is used to identify the sub-jet originating from the positively charged quark. The sub-jet charge is defined by a

weighted charge sum of sub-jet constituents:

$$Q_{sj}^{(\kappa)} = \sum_{i \in sj} Q_i (E^i / E_{sj})^\kappa, \quad (1)$$

where  $Q_i$  and  $E_i$  are the charge and energy of subjet constituent  $i$ , and the freely chosen parameter  $\kappa > 0$  is an exponent. A slightly modified definition based on a weighting by transverse momentum  $p_T$  is given by

$$Q_{sj}^{(\kappa)} = \frac{1}{(p_T^{\text{subjet}})^\kappa} \sum_{i \in sj} Q_i (p_T^i)^\kappa. \quad (2)$$

This definition is widely used by LHC experiments [25, 26]. Both definitions lead to very similar results in identifying the quark charge of the sub-jets from *jet2*. The first definition using energy based weighting has been used as default. Figure 6 (left) shows the subjet charge distributions for different values of  $\kappa$ , matching the subjets to the positively and negatively charged quark. For lower  $\kappa$  values the peaks of the two distributions move apart, at the cost of larger tails. For values of  $\kappa$  larger than 0.5 the discriminating power diminishes significantly, while for  $\kappa$  values below 0.20 the overlaps between both distributions are above 40%. For  $\kappa = 0.3$  the overlap of the  $Q_{sj}$  distributions is the smallest with 36.5% for both definitions. Thus  $\kappa = 0.3$  is used as default in the following when calculating the jet charges. Five different methods have been evaluated in order to select the positively charged quark:

1. Consider the sub-jet with the largest absolute jet charge value.
2. Consider the sub-jet with the largest energy.
3. Give preference to the sub-jet with the largest multiplicity of charged particles (pions, muons, electrons). If both sub-jets have the same multiplicity, then choose the sub-jet with the largest absolute jet charge value.
4. Consider the sub-jet with the largest charged energy fraction, defined as the energy sum carried by the charged particles divided by the total sub-jet energy.
5. Consider the sub-jet with the largest energy carried by charged particles.

If  $Q_{sj} > 0$ , the sub-jet is considered as positively charged quark, otherwise the other sub-jet is chosen. Figure 6 (right) shows the angle  $\theta_1$  between the chosen subjet and the Z-boson multiplied by the sign of the  $\cos \theta$  of the positively charged quark. In about 57% of events the correct hemisphere is identified for all five methods, with the first method providing the best correct assignment at a value slightly above 60%; it is subsequently used as default.

The normalised correlation matrices between the reconstructed and parton level for all three angles  $\cos \theta_1$ ,  $\cos \theta_2$ , and  $\phi$  are displayed in Fig. 7. In the case of  $\cos \theta_1$  diagonal elements dominate the matrix, illustrating that the subjet clustering of FastJet provides a suitable representation of the underlying quarks. A sizeable fraction of events populate the anti-diagonal, populated by events where the wrong sub-jet was chosen as positively charged quark. This anti-correlation has no impact on the derived values for the asymmetries as long as the transfer matrix is symmetric around an angle  $\theta_1$  of  $90^\circ$ . The definition of the asymmetry handles these anti-correlated cases in a similar manner as elements on the diagonal, as the positive and negative contributions of the asymmetry are determined by  $\text{sgn}(\cos(2 \cdot \theta_1))$ . As long as the transfer of events is symmetric with respect to  $\cos \theta_1$  the anti-correlation will pose no issue in the unfolding step. The spread around the (anti-) diagonal reflects the confusion term of assigning the reconstructed particles to the correct sub-jet. For  $\cos \theta_2$  in the overwhelming number of events the correct jet is chosen as direction for the H-jet, and as a consequence the matrix is almost diagonal. Since the angle  $\phi$  depends on the correct assignment of both the H jet and the positively charged quark direction, a similar behavior is observed as for the  $\cos \theta_1$  distribution.



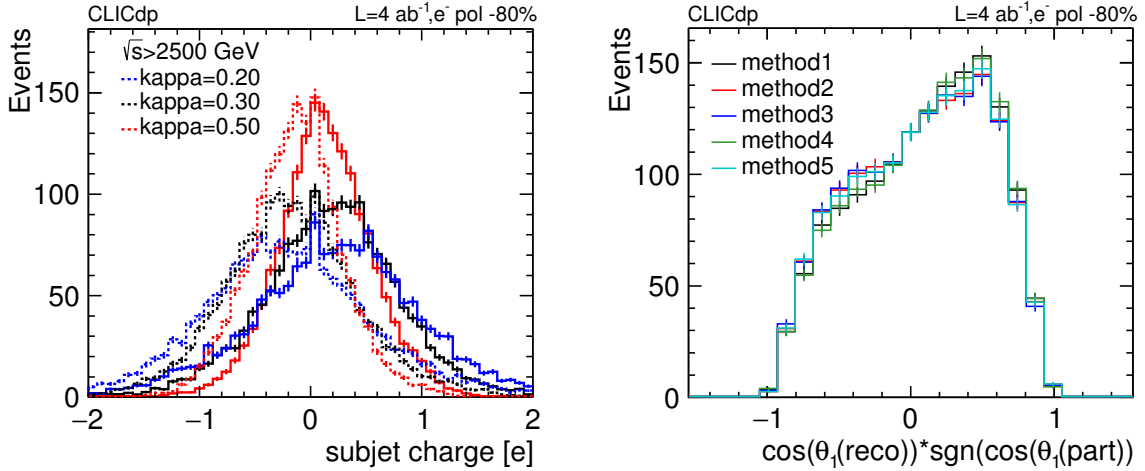


Figure 6: Impact of the weighting parameter  $\kappa$  on the subject charge distribution (left) for matched positively and negatively quarks from Z decays in HZ signal events. On the right the distribution of reconstructed  $\cos \theta_1$ , multiplied by the  $\text{sgn}(\cos \theta)$  of the positively charged quark from the Z-decay using five different selection methods. Events with the correctly reconstructed hemisphere will populate positive values.

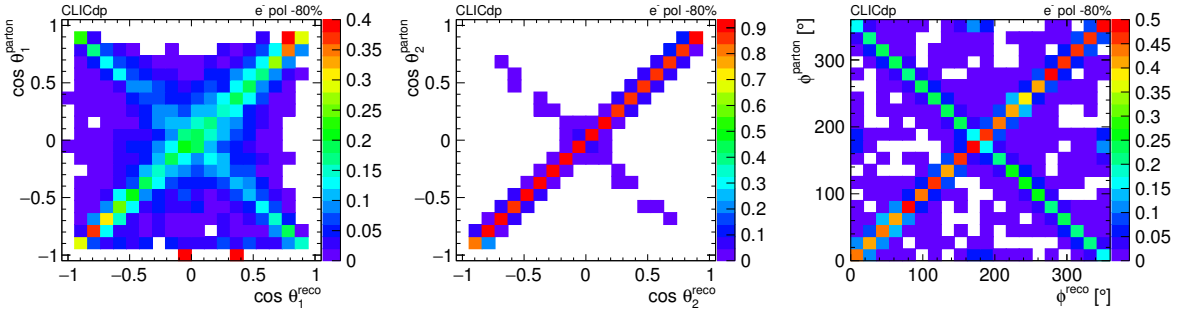


Figure 7: The normalised correlation matrices between the parton level and reconstructed level of the three angles of  $\cos \theta_1$  (left),  $\cos \theta_2$  (centre), and  $\phi$  (right) for HZ signal in events with negative electron beam polarisation.

#### 4. B-tagging in boosted H decays

The linear collider flavour identification (LCFIPlus) tool [27] is used to perform b-jet identification. The tools have been developed in the context of future  $e^+e^-$  linear colliders. The first step of LCFIPlus is the primary vertex finder, followed by the secondary vertex finder to identify  $b$  and  $c$  hadron decays, which are typically embedded in jets. In the second step the secondary vertices are assigned to jets, and isolated leptons are identified within the jet. These isolated leptons can originate from semileptonic decays of heavy flavour hadrons. Tracks from identified secondary vertices and leptons matched to these vertices are used as seeds for the third step of LCFIPlus, the so-called refined jet clustering. The input particles of the vertex finding and the subsequent jet finding step are the same. In case more particles are considered in the vertex clustering step than for the subsequent refined jet clustering, it can happen that the vertex itself creates its own jet without clustering any further particle specified as input for the refined clustering step. Thus it is not advised to perform secondary vertex finding using all PandoraPFOs clustered in both jets, and subsequently trying to assign the particles of the subjects to the identified vertices. Three different LCFIPlus settings have been investigated:



- use all PandoraPFOs clustered in both VLC jets as input for secondary vertexing and refined jet clustering, request two output jets. LCFIPlus provides in this case b-tagging information for each VLC jet.
- use all PandoraPFOs clustered in both VLC jets as input for secondary vertexing and refined jet clustering, request four output jets. LCFIPlus creates for each VLC jet at least one refined jet with b-tagging information.
- run LCFIPlus for each jet separately, use PandoraPFOs of each VLC jet separately as input for secondary vertexing and jet clustering, request two output jets. LCFIPlus creates for each VLC jet two refined subjects with b-tagging information.

The performance of the three settings is tested for the HZ events with  $H \rightarrow b\bar{b}$ . In all three settings, for the more massive jet one subject with a high b-tag probability is found, but less frequently two refined subjects with high b-tags. The third procedure provides refined subjects with the largest b-tag values for *jet1*, and is thus used throughout the analysis. As expected, for *jet2*, far less of the refined subjects are compatible with originating from a b-quark.

## 5. Monte Carlo simulation

Both signal and backgrounds samples are produced by WHIZARD 2.7.0, using luminosity spectra from GUINEAPIG interfaced by CIRCE2 with initial state radiation enabled. Parton shower and hadronisation are handled by PYTHIA 6. The DD4HEP detector description toolkit has been used to implement the simulated model of CLICdet in GEANT4, version 10.02p02, via the DDG4 package.

Backgrounds to all-hadronic HZ events originate from di-quark  $e^+e^- \rightarrow q\bar{q}$ , four-quark  $e^+e^- \rightarrow q\bar{q}q\bar{q}$  and six-quark  $e^+e^- \rightarrow q\bar{q}q\bar{q}q\bar{q}$  final states. In order to increase the statistics of the backgrounds at large effective  $\sqrt{s}$ , additional di-jet and four-quark samples have been produced with phase-space selections on the di-quark mass  $m_{q\bar{q}} > 1 \text{ TeV}$  and four quark mass  $m_{q\bar{q}q\bar{q}} > 2 \text{ TeV}$  respectively. It has been checked that all background events at large  $\sqrt{s}$  are originating from that particular phase-space. Table 1 lists the details of the produced samples for both negative and positive polarisation of 80% of the electron beam. The weight of each event is calculated under the assumption of luminosity sharing of the ratio 4:1 between the negative and positive polarisation of the electron beam, thus  $L_{-80\%} = 4 \text{ ab}^{-1}$  and  $L_{+80\%} = 1 \text{ ab}^{-1}$  are used as values for the integrated luminosity. The polarisation has a moderate impact on the HZ signal, decreasing the cross section by about 28% for positive compared to negative electron beam polarisation, a similar impact can be observed for the di-quark sample. The four-quark dataset cross section is largely reduced for positive polarisation by a factor of about 7.5. The six-quark dataset is split into 14 samples to cover all possible flavour combinations compatible with  $t\bar{t}$ . These datasets include the most relevant contributions from WWZ tri-boson production as well. In the Table 1 the six quark flavour combinations with the largest cross sections are shown. For the six quark dataset positive polarisation reduces the cross section considerably as well. Di-boson production from W W-fusion is expected to be negligible in the phase-space of this study.

## 6. Discriminating variables and signal selection

The jet mass distributions are most discriminating to differentiate between signal and background. The two dimensional distributions are shown in Fig. 8 for signal and background events. In order to provide a more signal-like selection for further processing a preselection is applied on the two-dimensional plane of the jet masses, selecting events which fall within a radius of 35 GeV around the Z-H mass point in the *jet2-jet1* mass plane. This cut retains about 85% of all HZ events, 89% of HZ events with  $H \rightarrow b\bar{b}$ . For the di-quark dataset the jet masses peak at considerably lower values. For the six-quark dataset the

Table 1: Signal and background datasets with  $y = d, s, b, L = 4 \text{ ab}^{-1}$  for  $P(e^-)=-80\%$ ,  $L = 1 \text{ ab}^{-1}$  for  $P(e^-)=+80\%$ :

process	additional cuts	Events	$\sigma[\text{fb}]$	Polarisation	event weight
$e^+e^- \rightarrow \text{HZ}$	-	114000	3.83	$P(e^-)=-80\%$	0.134
$e^+e^- \rightarrow \text{HZ}$	-	27840	2.76	$P(e^-)=+80\%$	0.0959
$e^+e^- \rightarrow q\bar{q}$	-	1549464	1269	$P(e^-)=-80\%$	3.28
$e^+e^- \rightarrow q\bar{q}$	-	388392	786	$P(e^-)=+80\%$	2.02
$e^+e^- \rightarrow q\bar{q}$	$m_{q\bar{q}} > 1 \text{ TeV}$	1519910	170.8	$P(e^-)=-80\%$	0.445
$e^+e^- \rightarrow q\bar{q}$	$m_{q\bar{q}} > 1 \text{ TeV}$	382464	73.5	$P(e^-)=+80\%$	0.192
$e^+e^- \rightarrow q\bar{q}q\bar{q}$	-	1915464	902	$P(e^-)=-80\%$	1.88
$e^+e^- \rightarrow q\bar{q}q\bar{q}$	-	479040	120	$P(e^-)=+80\%$	0.251
$e^+e^- \rightarrow q\bar{q}q\bar{q}$	$m_{q\bar{q}q\bar{q}} > 2 \text{ TeV}$	1522935	369.8	$P(e^-)=-80\%$	0.971
$e^+e^- \rightarrow q\bar{q}q\bar{q}$	$m_{q\bar{q}q\bar{q}} > 2 \text{ TeV}$	380451	49.2	$P(e^-)=+80\%$	0.129
$e^+e^- \rightarrow \text{dduyyu}$	-	456336	14.5	$P(e^-)=-80\%$	0.127
$e^+e^- \rightarrow \text{dduyyu}$	-	121200	5.01	$P(e^-)=+80\%$	0.0413
$e^+e^- \rightarrow \text{yyubbc}$	-	428405	13.3	$P(e^-)=-80\%$	0.124
$e^+e^- \rightarrow \text{yyubbc}$	-	123720	5.21	$P(e^-)=+80\%$	0.0421
$e^+e^- \rightarrow \text{sscbbc}$	-	330096	12.5	$P(e^-)=-80\%$	0.151
$e^+e^- \rightarrow \text{sscbbc}$	-	84240	4.89	$P(e^-)=+80\%$	0.0581

2D mass distribution has a maximum around the top-mass, as well as a sub-leading maximum around W and Z boson masses. For the four-quark dataset the mass peak is around the W and Z boson masses. The preselection cut on the 2D mass plane removes about 85% of di-quark, over 90% of six-quark, and about 62% of four-quark events as presented in Table 2. For events with large reconstructed centre-of-mass-energy,  $\sqrt{s} > 2500 \text{ GeV}$ , the amount of HZ events is 0.38% of all events for negative  $e^-$  polarisation, for events with positive  $e^-$  polarisation the signal purity is 1.5% without any further selection.

Table 2: Mass preselection efficiencies and event numbers for signal and background events, assuming an integrated luminosity of  $L = 4 \text{ ab}^{-1}$  for runs with negative polarisation  $P(e^-)=-80\%$ , and  $L = 1 \text{ ab}^{-1}$  for runs with positive polarisation  $P(e^-)=+80\%$ . All numbers are given for  $\sqrt{s} > 2500 \text{ GeV}$ :

process	Events neg. p.	Evts after cut neg. p.	Efficiency neg. p., in [%]	Events pos. p.	Evts after cut pos. p.	Efficiency pos. p., [in%]
$e^+e^- \rightarrow \text{HZ}, H \rightarrow b\bar{b}$	1740	1541	89	304	268	88
$e^+e^- \rightarrow \text{HZ}, \text{all H}$	2600	2210	85	458	388	85
$e^+e^- \rightarrow q\bar{q}$	172 000	25 019	15	18 600	2680	14
$e^+e^- \rightarrow q\bar{q}q\bar{q}$	248 000	91 100	37	8 450	3190	38
$e^+e^- \rightarrow q\bar{q}q\bar{q}q\bar{q}$	32 200	3190	9.9	3 090	145	4.7

After applying the preselection the following classes of variables have been considered:

- polar angles  $\theta$  of both leading jets: while the signal tends to be central, four- and six-quark events are peaked considerably more forward.
- b-tagging information of the leading jet: For the signal a very high b-tagging probability is observed, most events having values larger than 0.9. The background peaks at lower values close to 0. No large discriminating power is observed using c-tagging or light flavour tagging probability on the leading jets, probabilities for the sub-leading jet are very similar as well.

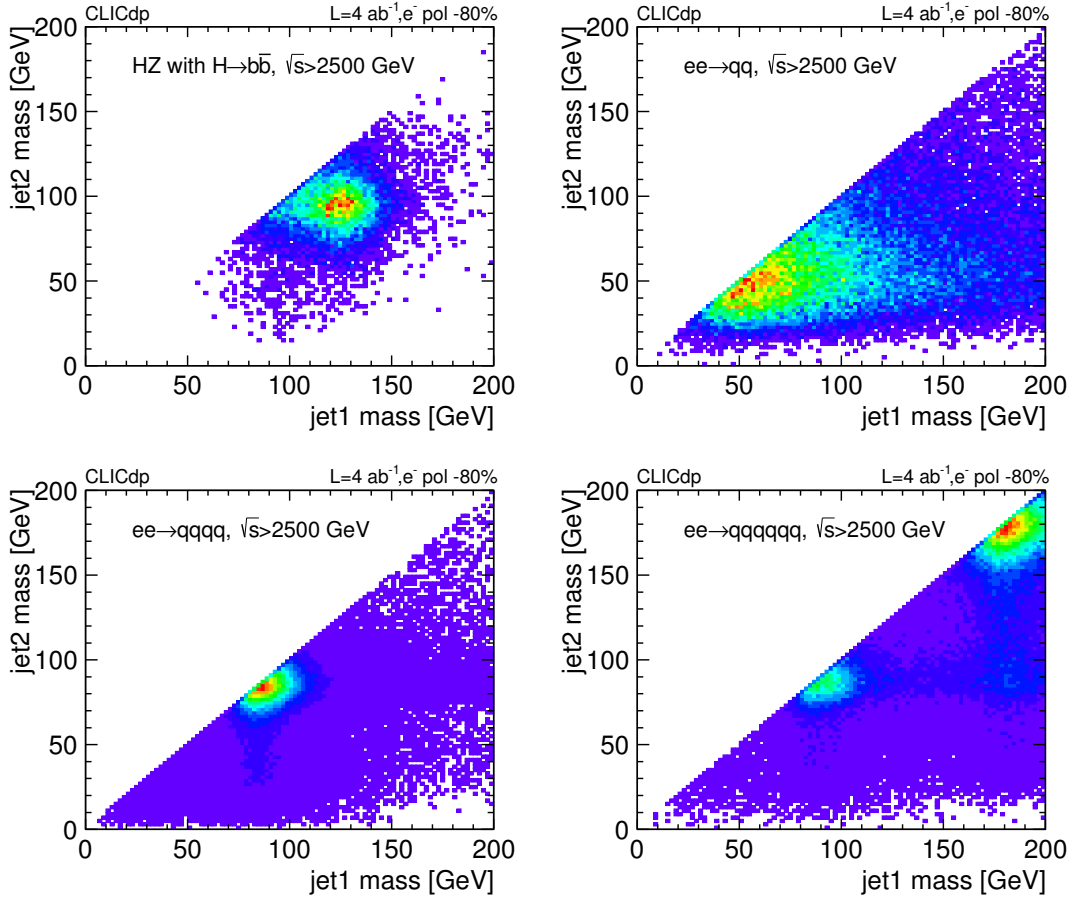


Figure 8: The two-dimensional mass plane of the leading vs the second leading mass for HZ (top left),  $e^+e^- \rightarrow q\bar{q}$  (top right),  $e^+e^- \rightarrow q\bar{q}q\bar{q}$  (bottom left), and  $e^+e^- \rightarrow qq\bar{q}\bar{q}q\bar{q}$  events (bottom right) with negative electron beam polarisation.

- event shape information, based on the three-jet resolution parameter  $y_{23}$ .
- jet substructure information of both jets, notably the N-subjettiness ratio  $\tau_{21} = \tau_2/\tau_1$  [28], and ratios between generalised jet energy correlation functions. These are correlation functions based on energies and pair wise angles between particles within jets [29]. Ratios between jet energy correlations lead to new jet substructure variables  $C_2^{(\beta)}$ ,  $C_3^{(\beta)}$ , and  $D_2^{(\beta)}$  [30]. In this analysis, a definition of jet energy correlations based on transverse momenta  $p_T$  and radial distances is used, with  $\beta = 1.0$  as weighting factor.

The identification targets to discriminate between background events and signal events. Signal events are defined as HZ events with  $H \rightarrow b\bar{b}$ , since at 3 TeV CLIC the coupling of H and b will be known to best accuracy, and systematic uncertainties on the other H decays have a smaller impact. In addition to the distributions listed above, the acoplanarity  $\Delta\phi(\text{jet1}, \text{jet2})$ , the four-jet resolution parameter  $y_{34}$ , the subjet merge clustering measures  $d_{12}$ ,  $d_{23}$ ,  $d_{34}$ , and energy correlation ratios  $N_2^{(\beta)}$ ,  $N_3^{(\beta)}$  [31] have been studied. These are found to lead to no further improvement in discriminating power.

Figures 9-13 display the most discriminating distributions after preselection for events with negative electron beam polarisation. Analogous plots for events with positive electron beam polarisation can be found in appendix A. The jet polar angle distributions of four quark and six-quark events after the preselection are peaked more forward, while for HZ both jet polar angle distributions are peaked in

the central region of the detector around  $\theta$  of  $90^\circ$ . While the signal has a high content of b-jets, the backgrounds are largely dominated by light flavour jets. Substructure variables are particularly powerful for discriminating between the one-prong structure of jets from  $e^+e^- \rightarrow q\bar{q}$  and the two-prong structure of jets from  $e^+e^- \rightarrow HZ$ .

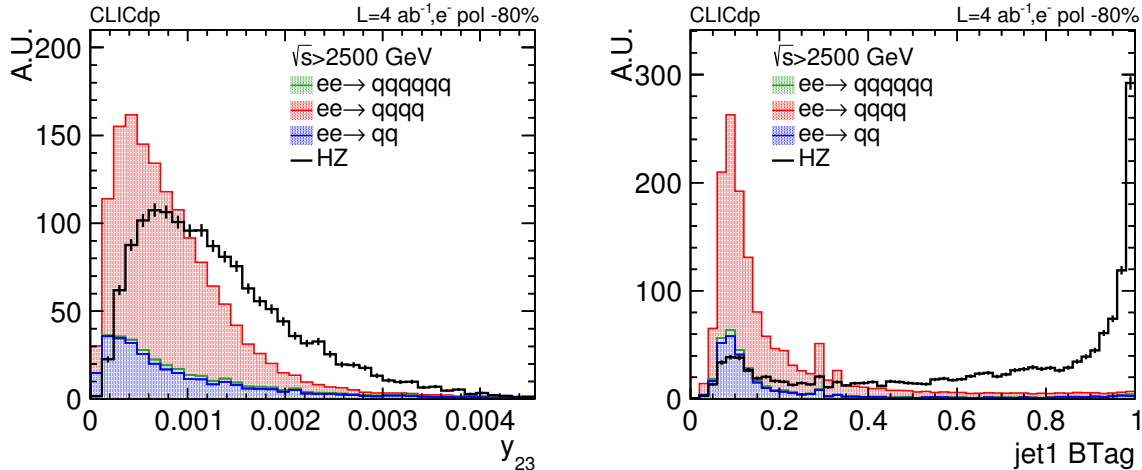


Figure 9: The three-jet resolution parameter  $y_{23}$  (left) and the b-tag distribution of the leading jet (left) for signal and background events with negative electron beam polarisation.

The background and signal discrimination is achieved using boosted decision trees as implemented in the Toolkit for MultiVariate data Analysis (TMVA) [32], integrated into ROOT [33]. Using adaptive boosting leads to slightly better results than using gradient boosting. In both cases the best results are achieved using the Gini-index as separation criteria. BDTs are trained separately for both polarisation states, restricting the signal to  $H \rightarrow b\bar{b}$  decays. Training the BDT on all full-hadronic H final states does not lead to any significant increase in events compared to using the  $H \rightarrow b\bar{b}$  only trained BDT. The angle  $\theta_1$  depends on the inner structure of  $jet2$ , particularly the jet substructure variables based on jet energy correlations. Including these substructure variables in the BDT leads to a slight bias for the asymmetry distribution  $A_{\theta_1}$  to larger negative values. Excluding these variables from the BDT training removes this bias with reconstructed  $A_{\theta_1}$  value very close to the parton level prediction, but at the cost of a larger amount of background, particularly from the di-quark dataset. Including substructure from the second jet leads to very similar  $A_{\theta_1}$  values for background and signal events. Removing these variables from the training leads to a considerable shift in  $A_{\theta_1}$  to lower negative values for background events.

Figure 14 shows the good agreement between the BDT score of events used to train the BDT and the other half of events, the testing dataset, for both polarisations. No sign of overtraining is observed. The significance of the HZ signal as well as the purity of the selection are shown as a function of the BDT score in Fig. 15 both for negative and positive polarisation final states.

## 7. Total cross section and angular distributions

The final event numbers are listed in Table 3. For events with negative electron beam polarisation a cut on the BDT score of  $BDT > 0.375$  achieves for all H decays a significance of about 22.5 with a purity of 57%. For events with positive beam polarisation data, a cut on the BDT score of  $BDT > 0.30$  achieves a significance of about 11.4, with a slightly higher purity of 72%. These numbers are equivalent to statistical precisions of about 4.4%, and 8.8% respectively. The higher purity is a result of the relatively lower background rates for positive electron beam polarisation, particularly from four-quark samples. Beyond  $HZ \rightarrow b\bar{b}$ , the selected other channels are H decays into  $W^+W^-$ ,  $\tau^+\tau^-$ , gg, and to a lesser

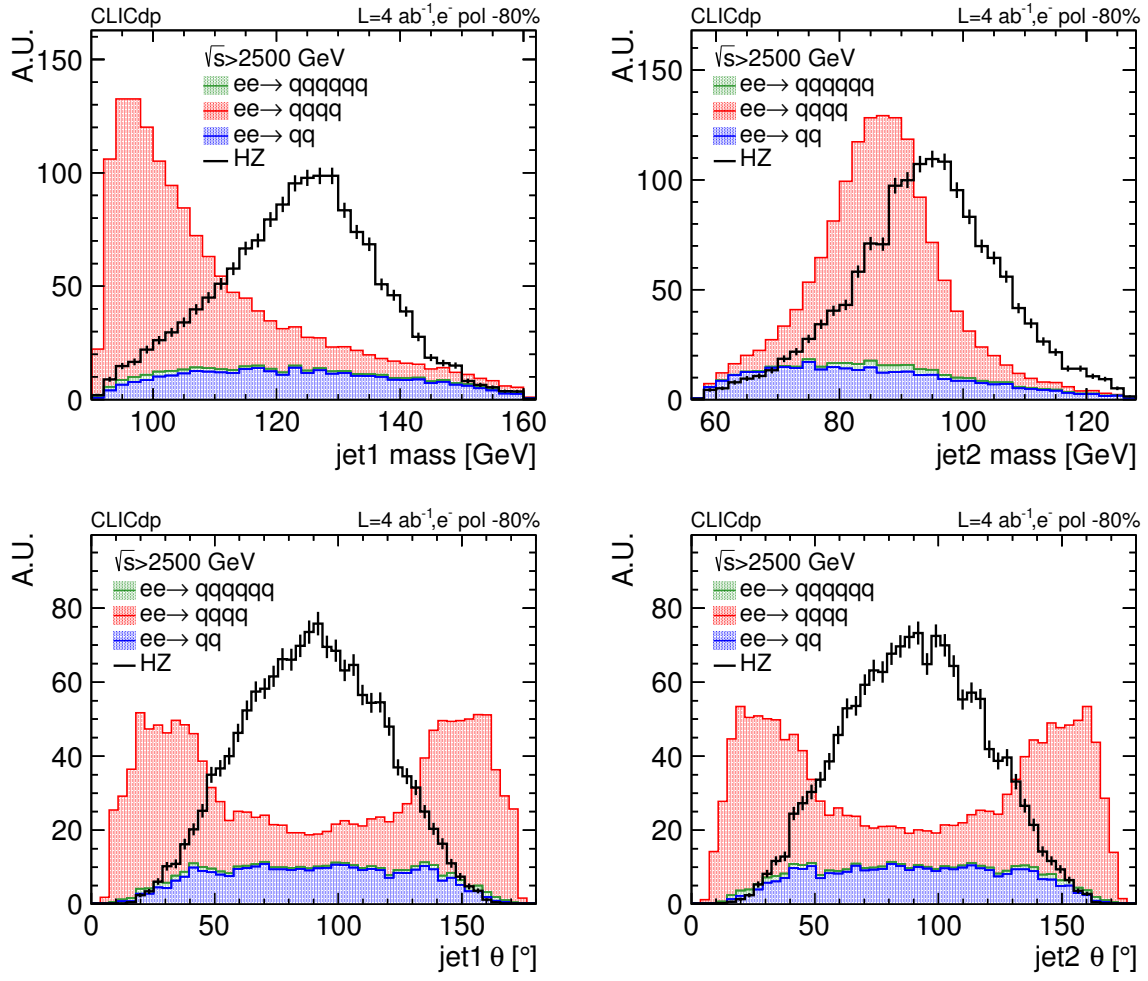


Figure 10: The jet mass (top) and polar angle distributions (bottom) for the leading (left) and subleading (right) jet for signal and background events with negative electron beam polarisation.

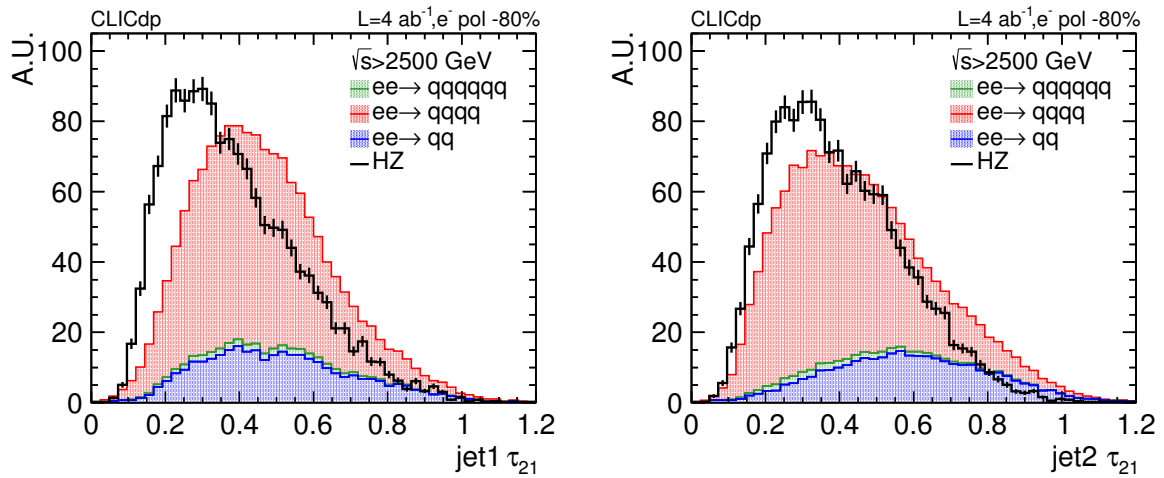


Figure 11: The N-subjettiness ratio  $\tau_{21}$  for the leading (left) and sub-leading jet (right) for signal and background events with negative electron beam polarisation.

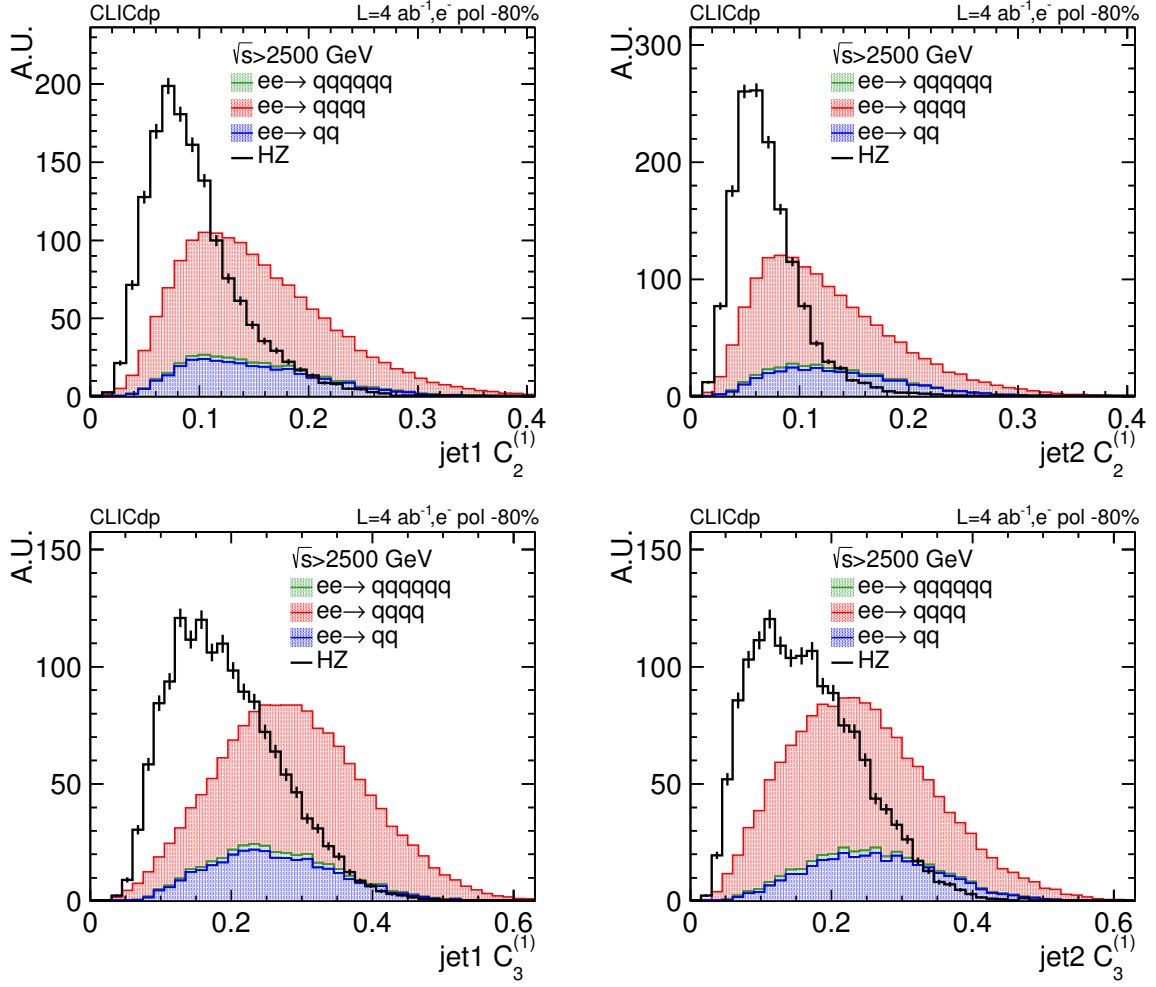


Figure 12: The jet energy correlation ratio distribution  $C_2^{(1)}$  (top) and  $C_3^{(1)}$  (bottom) for the leading (left) and sub-leading (right) jet for signal and background events with negative electron beam polarisation.

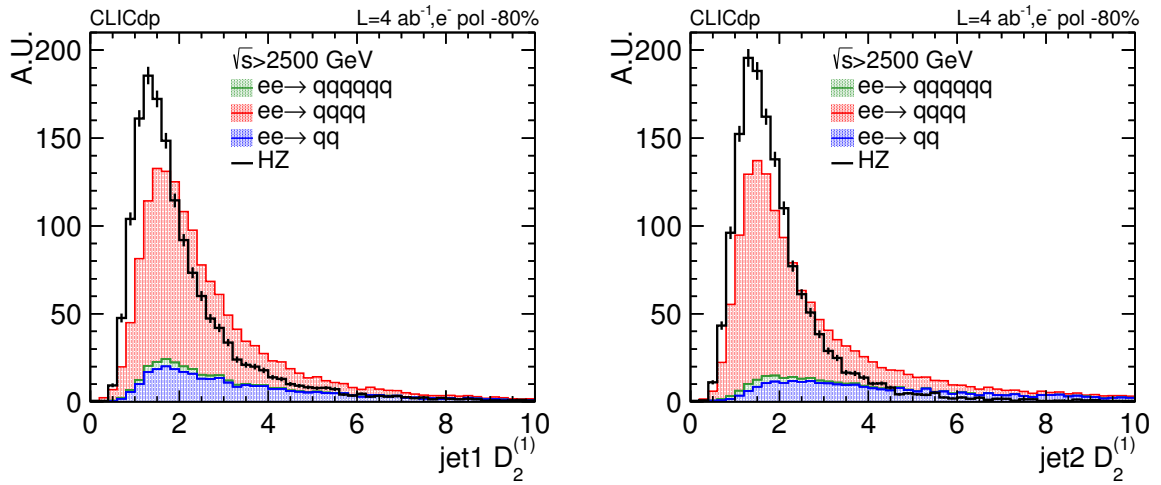


Figure 13: The jet energy correlation ratio  $D_2^{(1)}$  for the leading (left) and sub-leading jet (right) for signal and background events with negative electron beam polarisation.

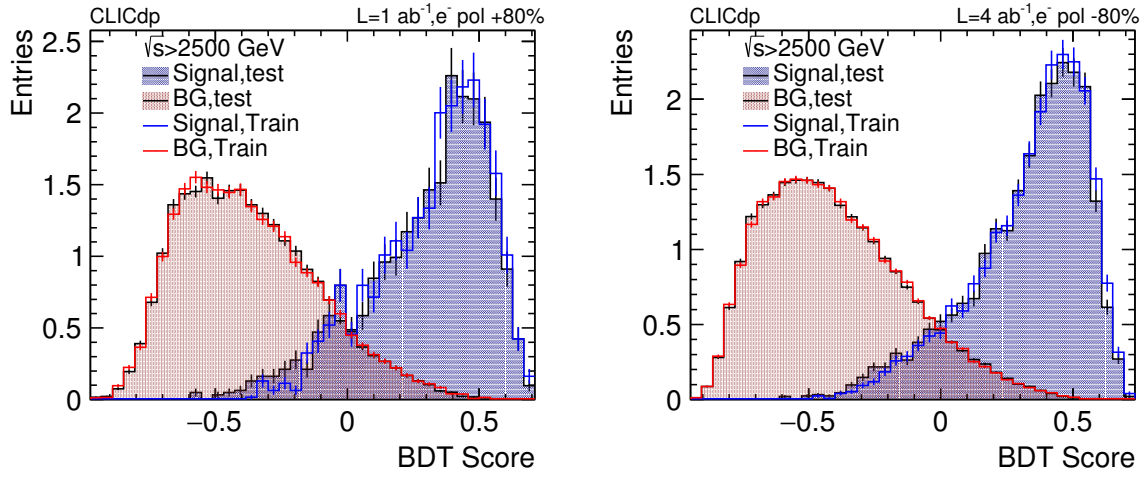


Figure 14: The distribution of the BDT score for positive (left) and negative (right) electron beam polarisation for the training and testing samples.

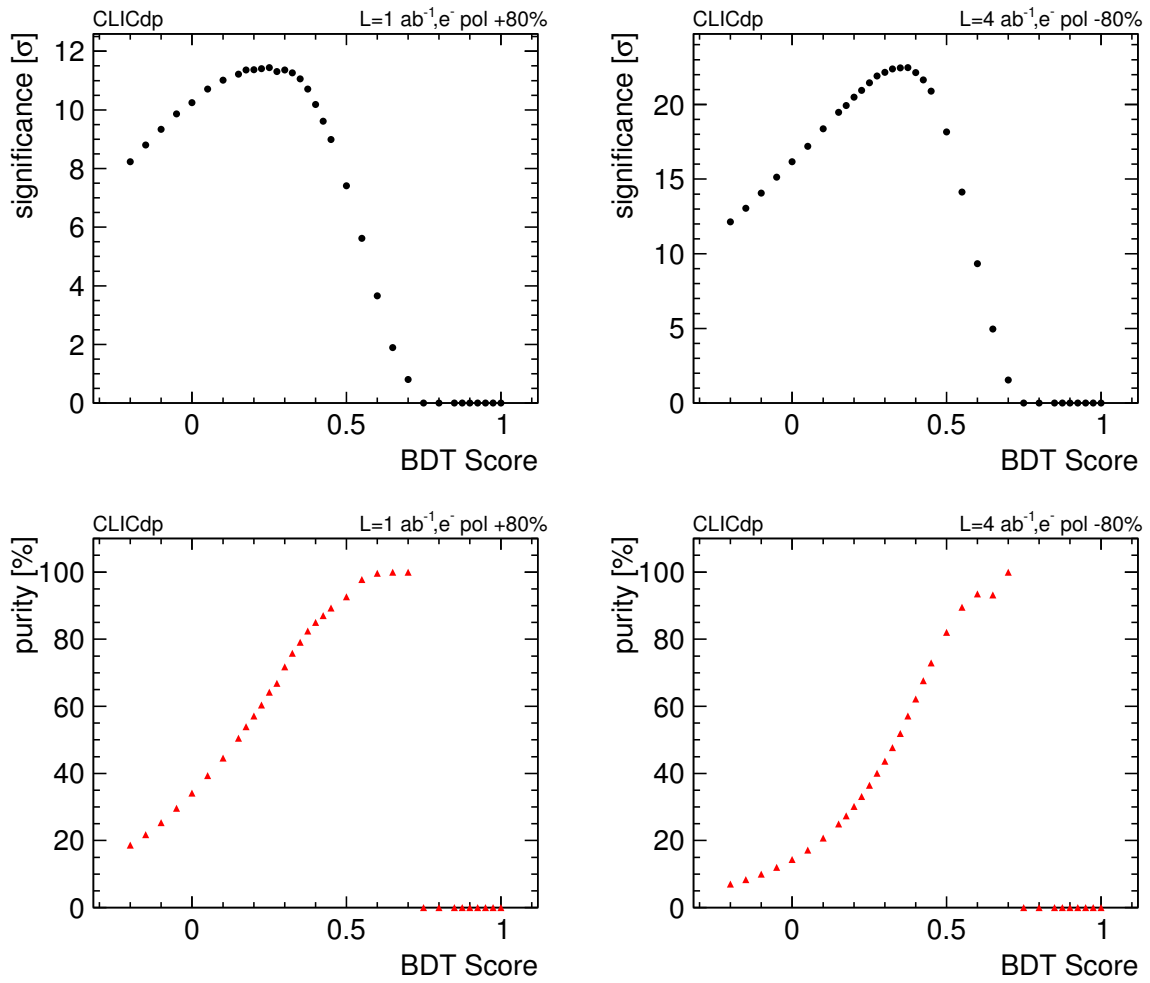


Figure 15: The signal significance as function of the BDT score for positive (upper left) and negative (upper right) electron beam polarisation as well as the corresponding signal purities.



extend into  $c\bar{c}$ . The combined uncertainty of 4.0% is in agreement with earlier estimates from a fast simulation study [4].

Table 3: Event numbers with purities and selection efficiencies after the final selection for signal and background events, assuming an integrated luminosity of  $L = 4 \text{ ab}^{-1}$  for runs with negative polarisation  $P(e^-)=-80\%$ , and  $L = 1 \text{ ab}^{-1}$  for runs with positive polarisation  $P(e^-)=+80\%$ . All numbers are given for  $\sqrt{s} > 2500 \text{ GeV}$ :

process	Events neg. p.	Purity neg. p., in [%]	Efficiency neg. p., in [%]	Events pos. p.	Purity pos. p., in [%]	Efficiency pos. p., in [%]
$e^+e^- \rightarrow \text{HZ}, \text{H} \rightarrow b\bar{b}$	811	52	47	162	64	53
$e^+e^- \rightarrow \text{HZ}, \text{all H}$	884	57	34	180	72	39
$e^+e^- \rightarrow q\bar{q}$	256	17	0.15	33.7	13	0.18
$e^+e^- \rightarrow q\bar{q}q\bar{q}$	335	22	0.12	30.8	12	0.36
$e^+e^- \rightarrow q\bar{q}q\bar{q}q\bar{q}$	71.1	4.6	0.22	6.28	2.5	0.20

The three reconstructed angular distributions of  $\cos\theta_1$ ,  $\cos\theta_2$ , and  $\phi$  are shown in Fig. 16 for HZ signal and background events. The lower plots display the ratio between background and signal events. Background events tend to be rather flat with respect to signal distributions after applying the signal selection. Thus it is expected that the background contamination has a mild effect on the extracted asymmetry values.

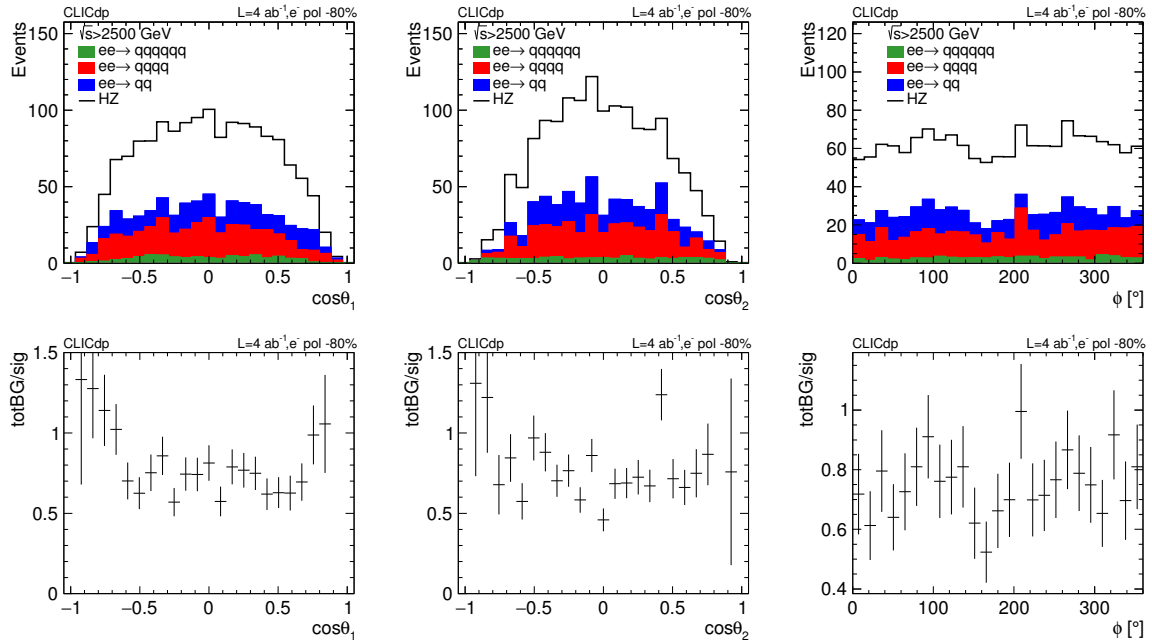


Figure 16: The three reconstructed angular distributions of  $\cos\theta_1$  (left),  $\cos\theta_2$  (centre), and  $\phi$  (right) for signal and background events with negative electron beam polarisation. The lower plots show the ratios between background and signal events.

Tables 4 and 5 list the asymmetries with their statistical uncertainties separately for HZ events with  $\text{HZ} \rightarrow b\bar{b}$ , HZ with all H decays, the asymmetries for the sum of signal and background events, the asymmetries on reconstruction level after mass preselection, and the values for parton-level at large  $\sqrt{s}$ . The asymmetries are considered separately for both polarisation schemes for the electron beam. Most asymmetry values are consistent with 0, the values for  $A_{\theta_1}$  are shifted to more negative values of larger

than  $-0.80$ , compared to partonic values of around  $-0.76$ . This slight bias is introduced by the cuts on the substructure observables of the second jet. The value of  $A_{\theta_1}$  depends on  $\sqrt{s}$ , e.g for the lowest energy stage values of about  $-0.6$  are predicted. The statistical uncertainties of values extracted for events with positive electron beam polarisation is roughly twice as large as the uncertainties for event with negative electron beam polarisation.

Table 4: Extracted values for asymmetry observables for signal and background events, assuming an integrated luminosity of  $L = 4 \text{ ab}^{-1}$  for runs with negative polarisation  $P(e^-)=-80\%$ . All numbers are given for  $\sqrt{s} > 2500 \text{ GeV}$ :

Asymmetry	$e^+e^- \rightarrow \text{HZ}$ $\text{H} \rightarrow b\bar{b}$	$e^+e^- \rightarrow \text{HZ}$ all H	Backgrounds	$e^+e^- \rightarrow \text{HZ}$ and BKG	Parton Level
$A_{c\theta_1, c\theta_2}$	$0.019 \pm 0.035$	$0.021 \pm 0.034$	$0.028 \pm 0.039$	$0.024 \pm 0.025$	$-0.021 \pm 0.019$
$A_{\theta_1}$	$-0.834 \pm 0.019$	$-0.837 \pm 0.018$	$-0.760 \pm 0.025$	$-0.804 \pm 0.015$	$-0.765 \pm 0.012$
$A_{\phi}^{(1)}$	$-0.002 \pm 0.035$	$-0.004 \pm 0.034$	$-0.050 \pm 0.039$	$-0.024 \pm 0.026$	$-0.005 \pm 0.019$
$A_{\phi}^{(2)}$	$-0.014 \pm 0.035$	$-0.011 \pm 0.034$	$-0.000 \pm 0.039$	$-0.006 \pm 0.026$	$-0.037 \pm 0.019$
$A_{\phi}^{(3)}$	$-0.001 \pm 0.035$	$-0.004 \pm 0.034$	$0.007 \pm 0.039$	$0.001 \pm 0.026$	$0.003 \pm 0.019$
$A_{\phi}^{(4)}$	$-0.036 \pm 0.035$	$-0.037 \pm 0.034$	$-0.07' \pm 0.039$	$-0.049 \pm 0.026$	$-0.015 \pm 0.019$

Table 5: Extracted values for asymmetry observables for signal and background events, assuming an integrated luminosity of  $L = 1 \text{ ab}^{-1}$  for runs with positive polarisation  $P(e^-)=+80\%$ . All numbers are given for  $\sqrt{s} > 2500 \text{ GeV}$ :

Asymmetry	$e^+e^- \rightarrow \text{HZ}$ $\text{H} \rightarrow b\bar{b}$	$e^+e^- \rightarrow \text{HZ}$ all H	Backgrounds	$e^+e^- \rightarrow \text{HZ}$ and BKG	Parton Level
$A_{c\theta_1, c\theta_2}$	$-0.015 \pm 0.079$	$-0.019 \pm 0.075$	$-0.035 \pm 0.119$	$-0.027 \pm 0.063$	$-0.021 \pm 0.046$
$A_{\theta_1}$	$-0.829 \pm 0.044$	$-0.835 \pm 0.041$	$-0.713 \pm 0.083$	$-0.801 \pm 0.038$	$-0.761 \pm 0.030$
$A_{\phi}^{(1)}$	$0.015 \pm 0.079$	$0.009 \pm 0.075$	$-0.102 \pm 0.118$	$-0.022 \pm 0.063$	$0.021 \pm 0.046$
$A_{\phi}^{(2)}$	$0.011 \pm 0.079$	$0.007 \pm 0.075$	$-0.011 \pm 0.119$	$0.002 \pm 0.063$	$0.051 \pm 0.046$
$A_{\phi}^{(3)}$	$0.059 \pm 0.079$	$0.058 \pm 0.074$	$0.014 \pm 0.119$	$0.046 \pm 0.063$	$0.041 \pm 0.046$
$A_{\phi}^{(4)}$	$-0.053 \pm 0.079$	$-0.039 \pm 0.074$	$-0.015 \pm 0.119$	$-0.037 \pm 0.063$	$0.004 \pm 0.046$

## 8. Systematic uncertainties

Systematic uncertainties are hard to estimate without a detailed knowledge on the precise technical details of the detector. At this stage the impact of sources of potential systematic uncertainties of relevance for this final state is discussed. The total luminosity is expected to be measured to an accuracy of a few per mille with the luminometer of CLICdet, using Bhabha scattering events [34, 35]. The rate of events in the high-energy  $\sqrt{s}$  region depends on the luminosity spectrum. The relative uncertainty of events with  $\sqrt{s}$  close to the nominal centre-of-mass energy of 3 TeV is about 0.2% [36]. The expected uncertainty on the beam polarisation is on the level of 0.2% [37]. These three sources lead to negligible effects compared to the statistical uncertainty. An uncertainty on the jet energy scale of 1% leads to a systematic uncertainty of 0.08% (0.2%) for events with negative (positive) electron beam polarisation. The uncertainty on the b-tagging shape is estimated by reweighting b-tagging values with linear slope, which increases b-tagging values of 0 by 1% and decreases b-tagging values of 1 by 1% and vice versa. The reweighted shapes are normalized, keeping the number of events after the preselection on the jet masses constant. This leads to

a systematic uncertainty of about 0.9% on the cross section. Both the jet energy scale uncertainty of 1% and the b-tagging shape uncertainty lead to negligible effects on the errors of the asymmetries and the value of  $A_{\theta_1}$ .

## 9. Summary and conclusions

A study of Higgs production from HZ with hadronic Z decays has been presented at high centre-of-mass energies at the 3 TeV energy stage of CLIC. At these high energies hadronically decaying boosted H and Z bosons are identified using boosted jets and jet substructure variables. This is the first analysis with the new detector model CLICdet and the new software. The analysis profits from the excellent jet energy and mass reconstruction of CLICdet based on high granularity calorimeters optimised for particle flow algorithms. The statistical uncertainty on the cross section of all-hadronic high-energy HZ production is about 4.4% for events with negative electron beam polarisation, and 8.8% for events with positive electron beam polarisation, and a combined uncertainty of 4.0%. Angular asymmetries, which are particularly sensitive to deviations from the Standard Model in HZ production, have been extracted on reconstructed level. For most observables signal and background events are shape-wise similar. Backgrounds tend to produce more forward events for the  $\cos \theta_1$  distribution. This counteracts the bias of the event selection on the signal, which is more efficient for central  $\cos \theta_1$  values.

## Acknowledgements

This work benefited from services provided by the ILC Virtual Organisation, supported by the national resource providers of the EGI Federation. This research was done using resources provided by the Open Science Grid, which is supported by the National Science Foundation and the U.S. Department of Energy's Office of Science. This project has received funding from the European Union's Horizon 2020 Research and Innovation programme under Grant Agreement no. 654168.

## References

- [1] M. Aicheler et al., CLIC Collaboration, *The Compact Linear Collider (CLIC) - Project Implementation Plan* (2019), DOI: 10.23731/CYRM-2018-004, arXiv: 1903.08655 [physics.acc-ph].
- [2] M. J. Boland et al., CLIC and CLICdp Collaborations, *Updated baseline for a staged Compact Linear Collider* (2016), ed. by P. Lebrun et al., DOI: 10.5170/CERN-2016-004, arXiv: 1608.07537 [physics.acc-ph].
- [3] H. Abramowicz et al., *Higgs Physics at the CLIC electron-positron linear collider*, Eur. Phys. J. **C77** (2017) 475, DOI: 10.1140/epjc/s10052-017-4968-5, arXiv: 1608.07538 [hep-ex].
- [4] J. Ellis et al., *Dimension-6 Operator Analysis of the CLIC Sensitivity to New Physics*, JHEP **05** (2017) 096, DOI: 10.1007/JHEP05(2017)096, arXiv: 1701.04804 [hep-ph].
- [5] J. de Blas et al., *Higgs Boson Studies at Future Particle Colliders* (2019), arXiv: 1905.03764 [hep-ph].
- [6] J. De Blas et al., *On the future of Higgs, electroweak and diboson measurements at lepton colliders* (2019), arXiv: 1907.04311 [hep-ph].

- 
- [7] M. Beneke, D. Boito, Y.-M. Wang, *Anomalous Higgs couplings in angular asymmetries of  $H \rightarrow Z\ell^+\ell^-$  and  $e^+e^- \rightarrow HZ$* , JHEP **11** (2014) 028, DOI: [10.1007/JHEP11\(2014\)028](https://doi.org/10.1007/JHEP11(2014)028), arXiv: [1406.1361](https://arxiv.org/abs/1406.1361) [hep-ph].
- [8] J. de Blas et al., *The CLIC Potential for New Physics* (2018), DOI: [10.23731/CYRM-2018-003](https://doi.org/10.23731/CYRM-2018-003), arXiv: [1812.02093](https://arxiv.org/abs/1812.02093) [hep-ph].
- [9] A. Robson, P. Roloff, *Updated CLIC luminosity staging baseline and Higgs coupling prospects* (2018), arXiv: [1812.01644](https://arxiv.org/abs/1812.01644) [hep-ex].
- [10] N. Alipour Tehrani et al., *CLICdet: The post-CDR CLIC detector model* (2017), CLICdp-Note-2017-001, URL: <https://cds.cern.ch/record/2254048>.
- [11] D. Arominski et al., CLICdp Collaboration, *A detector for CLIC: main parameters and performance* (2018), arXiv: [1812.07337](https://arxiv.org/abs/1812.07337) [physics.ins-det].
- [12] M. Frank et al., *DDG4 A Simulation Framework based on the DD4hep Detector Description Toolkit*, J. Phys. Conf. Ser. **664** (2015) 072017, DOI: [10.1088/1742-6596/664/7/072017](https://doi.org/10.1088/1742-6596/664/7/072017).
- [13] A. Sailer et al., CLICdp and ILD Collaborations, *DD4Hep based event reconstruction*, J. Phys. Conf. Ser. **898** (2017) 042017, DOI: [10.1088/1742-6596/898/4/042017](https://doi.org/10.1088/1742-6596/898/4/042017).
- [14] S. Agostinelli et al., GEANT4 Collaboration, *GEANT4: A Simulation toolkit*, Nucl. Instrum. Meth. **A506** (2003) 250, DOI: [10.1016/S0168-9002\(03\)01368-8](https://doi.org/10.1016/S0168-9002(03)01368-8).
- [15] D. Schulte, *Beam-Beam Simulations with GUINEA-PIG* (1999), URL: <https://cds.cern.ch/record/382453>.
- [16] E. Brondolin et al., *Conformal Tracking for all-silicon trackers at future electron-positron colliders*, submitted to Nucl. Instrum. Meth. A (2019), arXiv: [1908.00256](https://arxiv.org/abs/1908.00256) [physics.ins-det].
- [17] H. Tran et al., *Software compensation in Particle Flow reconstruction*, Eur. Phys. J. **C77** (2017) 698, DOI: [10.1140/epjc/s10052-017-5298-3](https://doi.org/10.1140/epjc/s10052-017-5298-3), arXiv: [1705.10363](https://arxiv.org/abs/1705.10363) [physics.ins-det].
- [18] J. S. Marshall, M. A. Thomson, *The Pandora Software Development Kit for Pattern Recognition*, Eur. Phys. J. **C75** (2015) 439, DOI: [10.1140/epjc/s10052-015-3659-3](https://doi.org/10.1140/epjc/s10052-015-3659-3), arXiv: [1506.05348](https://arxiv.org/abs/1506.05348) [physics.data-an].
- [19] J. S. Marshall, A. Münnich, M. A. Thomson, *Performance of Particle Flow Calorimetry at CLIC*, Nucl. Instrum. Meth. **A700** (2013) 153, DOI: [10.1016/j.nima.2012.10.038](https://doi.org/10.1016/j.nima.2012.10.038), arXiv: [1209.4039](https://arxiv.org/abs/1209.4039) [physics.ins-det].
- [20] M. Cacciari, G. P. Salam, G. Soyez, *FastJet User Manual*, Eur. Phys. J. **C72** (2012) 1896, DOI: [10.1140/epjc/s10052-012-1896-2](https://doi.org/10.1140/epjc/s10052-012-1896-2), arXiv: [1111.6097](https://arxiv.org/abs/1111.6097) [hep-ph].
- [21] M. Boronat et al., *Jet reconstruction at high-energy electron-positron colliders*, Eur. Phys. J. **C78** (2018) 144, DOI: [10.1140/epjc/s10052-018-5594-6](https://doi.org/10.1140/epjc/s10052-018-5594-6), arXiv: [1607.05039](https://arxiv.org/abs/1607.05039) [hep-ex].
- [22] L. Linssen et al., eds., *CLIC Conceptual Design Report: Physics and Detectors at CLIC*, CERN-2012-003, CERN, 2012, arXiv: [1202.5940](https://arxiv.org/abs/1202.5940) [physics.ins-det].
- [23] N. Craig et al., *Beyond Higgs Couplings: Couplings: Probing the Higgs with Angular Observables at Future  $e^+e^-$  Colliders*, JHEP **03** (2016) 050, DOI: [10.1007/JHEP03\(2016\)050](https://doi.org/10.1007/JHEP03(2016)050), arXiv: [1512.06877](https://arxiv.org/abs/1512.06877) [hep-ph].

- 
- [24] G. Durieux et al., *The leptonic future of the Higgs*, JHEP **09** (2017) 014, DOI: [10.1007/JHEP09\(2017\)014](https://doi.org/10.1007/JHEP09(2017)014), arXiv: [1704.02333](https://arxiv.org/abs/1704.02333) [hep-ph].
- [25] A. M. Sirunyan et al., CMS Collaboration, *Measurements of jet charge with dijet events in pp collisions at  $\sqrt{s} = 8$  TeV*, JHEP **10** (2017) 131, DOI: [10.1007/JHEP10\(2017\)131](https://doi.org/10.1007/JHEP10(2017)131), arXiv: [1706.05868](https://arxiv.org/abs/1706.05868) [hep-ex].
- [26] G. Aad et al., ATLAS Collaboration, *Measurement of jet charge in dijet events from  $\sqrt{s}=8$  TeV pp collisions with the ATLAS detector*, Phys. Rev. **D93** (2016) 052003, DOI: [10.1103/PhysRevD.93.052003](https://doi.org/10.1103/PhysRevD.93.052003), arXiv: [1509.05190](https://arxiv.org/abs/1509.05190) [hep-ex].
- [27] T. Suehara, T. Tanabe, *LCFIPlus: A Framework for Jet Analysis in Linear Collider Studies*, Nucl. Instrum. Meth. **A808** (2016) 109, DOI: [10.1016/j.nima.2015.11.054](https://doi.org/10.1016/j.nima.2015.11.054), arXiv: [1506.08371](https://arxiv.org/abs/1506.08371) [physics.ins-det].
- [28] J. Thaler, K. Van Tilburg, *Identifying Boosted Objects with  $N$ -subjettiness*, JHEP **03** (2011) 015, DOI: [10.1007/JHEP03\(2011\)015](https://doi.org/10.1007/JHEP03(2011)015), arXiv: [1011.2268](https://arxiv.org/abs/1011.2268) [hep-ph].
- [29] A. J. Larkoski, G. P. Salam, J. Thaler, *Energy Correlation Functions for Jet Substructure*, JHEP **06** (2013) 108, DOI: [10.1007/JHEP06\(2013\)108](https://doi.org/10.1007/JHEP06(2013)108), arXiv: [1305.0007](https://arxiv.org/abs/1305.0007) [hep-ph].
- [30] A. J. Larkoski, I. Moult, D. Neill, *Power Counting to Better Jet Observables*, JHEP **12** (2014) 009, DOI: [10.1007/JHEP12\(2014\)009](https://doi.org/10.1007/JHEP12(2014)009), arXiv: [1409.6298](https://arxiv.org/abs/1409.6298) [hep-ph].
- [31] I. Moult, L. Necib, J. Thaler, *New Angles on Energy Correlation Functions*, JHEP **12** (2016) 153, DOI: [10.1007/JHEP12\(2016\)153](https://doi.org/10.1007/JHEP12(2016)153), arXiv: [1609.07483](https://arxiv.org/abs/1609.07483) [hep-ph].
- [32] A. Hoecker et al., *TMVA: Toolkit for Multivariate Data Analysis*, PoS ACAT (2007) 040, arXiv: [physics/0703039](https://arxiv.org/abs/physics/0703039).
- [33] I. Antcheva et al., *ROOT: A C++ framework for petabyte data storage, statistical analysis and visualization*, Comput. Phys. Commun. **180** (2009) 2499, DOI: [10.1016/j.cpc.2009.08.005](https://doi.org/10.1016/j.cpc.2009.08.005), arXiv: [1508.07749](https://arxiv.org/abs/1508.07749) [physics.data-an].
- [34] S. Lukić et al., *Correction of beam-beam effects in luminosity measurement in the forward region at CLIC*, JINST **8** (2013) P05008, DOI: [10.1088/1748-0221/8/05/P05008](https://doi.org/10.1088/1748-0221/8/05/P05008), arXiv: [1301.1449](https://arxiv.org/abs/1301.1449) [physics.acc-ph].
- [35] I. Božović-Jelisavčić et al., *Luminosity measurement at ILC*, JINST **8** (2013) P08012, DOI: [10.1088/1748-0221/8/08/P08012](https://doi.org/10.1088/1748-0221/8/08/P08012), arXiv: [1304.4082](https://arxiv.org/abs/1304.4082) [physics.acc-ph].
- [36] S. Poss, A. Sailer, *Luminosity Spectrum Reconstruction at Linear Colliders*, Eur. Phys. J. **C74** (2014) 2833, DOI: [10.1140/epjc/s10052-014-2833-3](https://doi.org/10.1140/epjc/s10052-014-2833-3), arXiv: [1309.0372](https://arxiv.org/abs/1309.0372) [physics.ins-det].
- [37] G. Wilson, *Beam Polarization Measurement Using Single Bosons with Missing Energy*, International Workshop on Future Linear Colliders (LCWS12), 2012.

## A. Distribution of events with positive electron beam polarisation

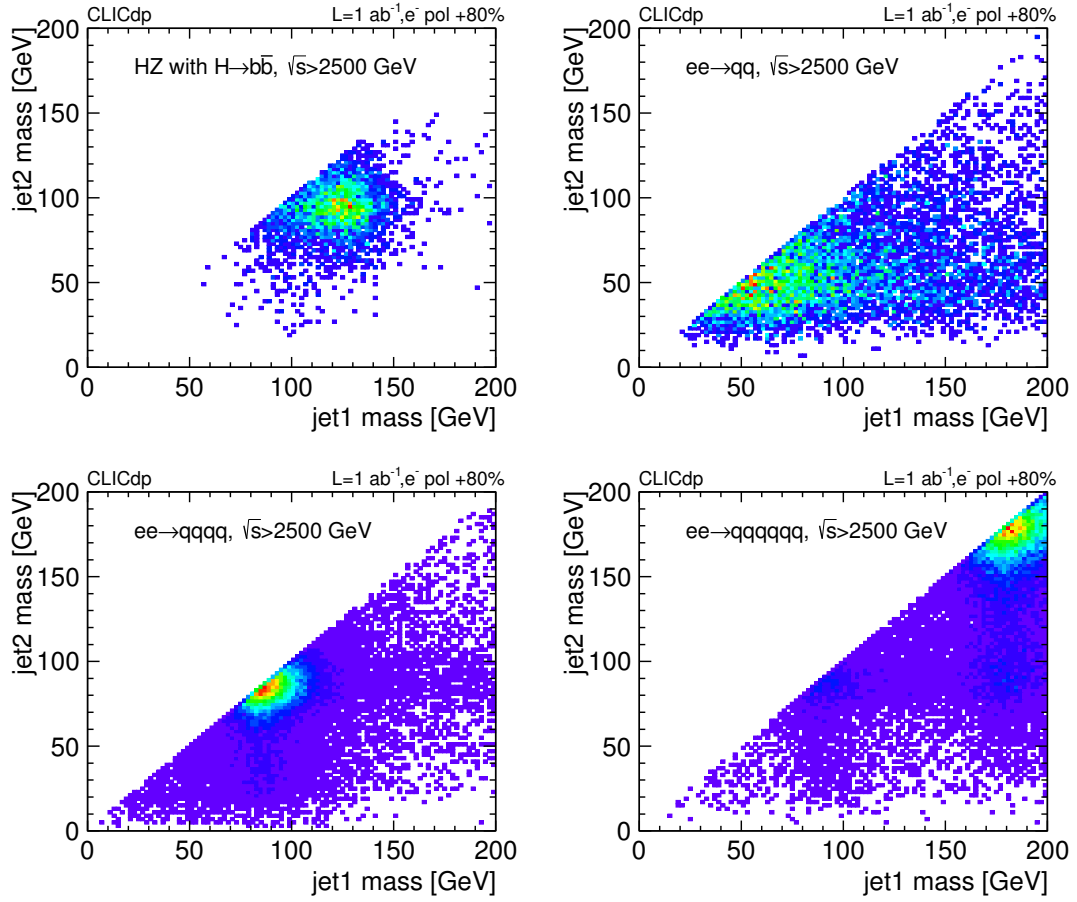


Figure 17: The two-dimensional mass plane of the leading vs the second leading mass for HZ (top left),  $e^+e^- \rightarrow q\bar{q}$  (top right),  $e^+e^- \rightarrow q\bar{q}q\bar{q}$  (bottom left), and  $e^+e^- \rightarrow qqqqqq$  events (bottom right) with positive electron beam polarisation.

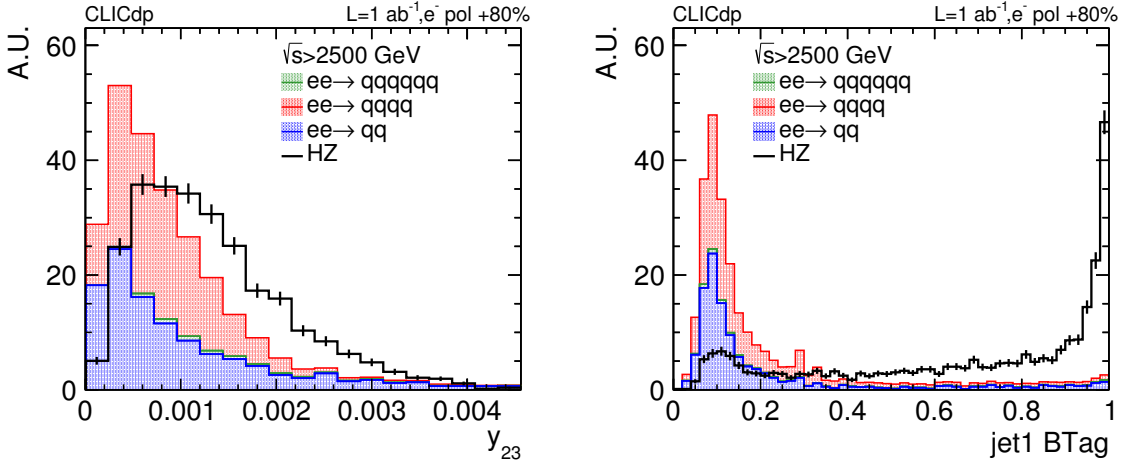


Figure 18: The three-jet resolution parameter  $y_{23}$  (left) and the b-tag distribution of the leading jet (right) for signal and background events with positive electron beam polarisation after the preselection on jet masses.

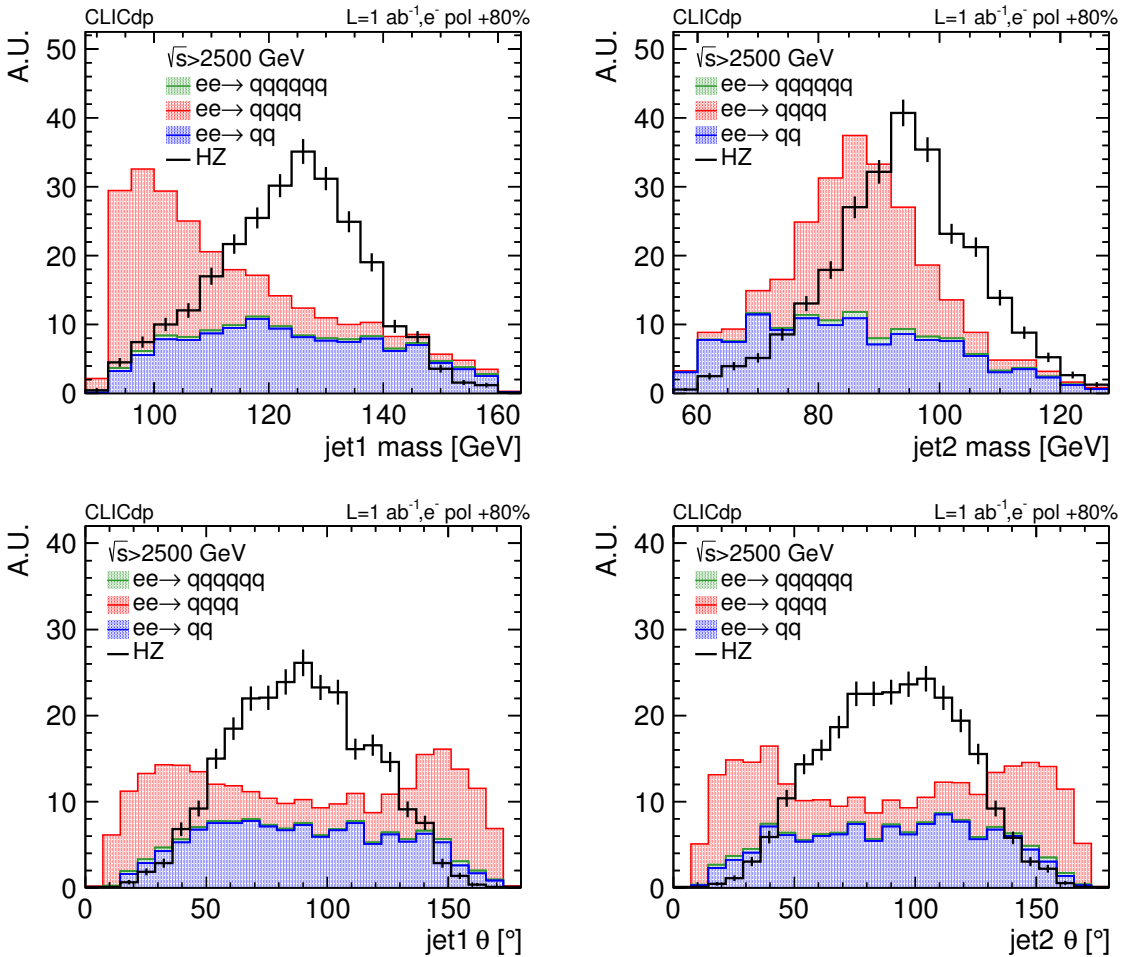


Figure 19: The jet mass (top) and polar angle distributions (bottom) for the leading (left) and subleading (right) jet for signal and background events with positive electron beam polarisation after the preselection on jet masses.



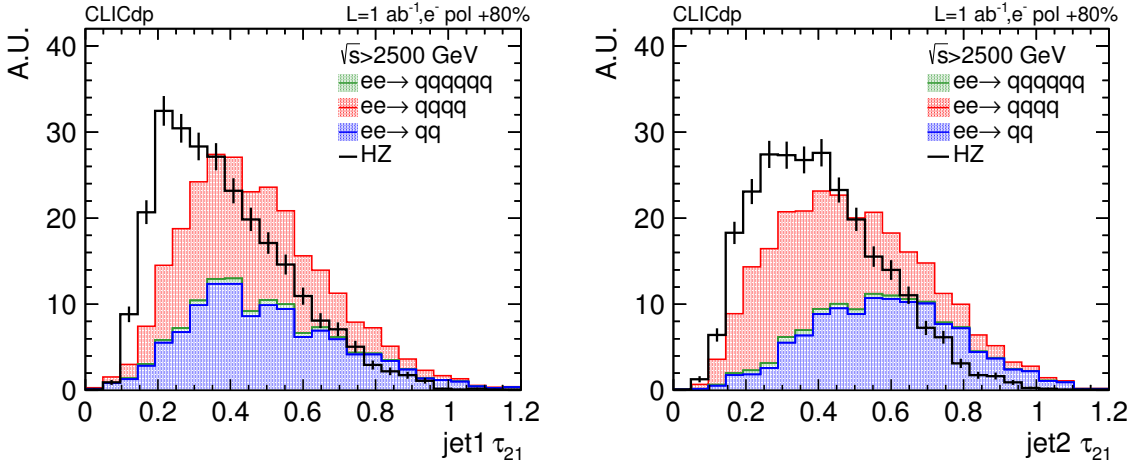


Figure 20: The N-subjettiness ratio  $\tau_{21}$  for the leading (left) and sub-leading jet (right) for signal and background events with positive electron beam polarisation after the preselection on jet masses.

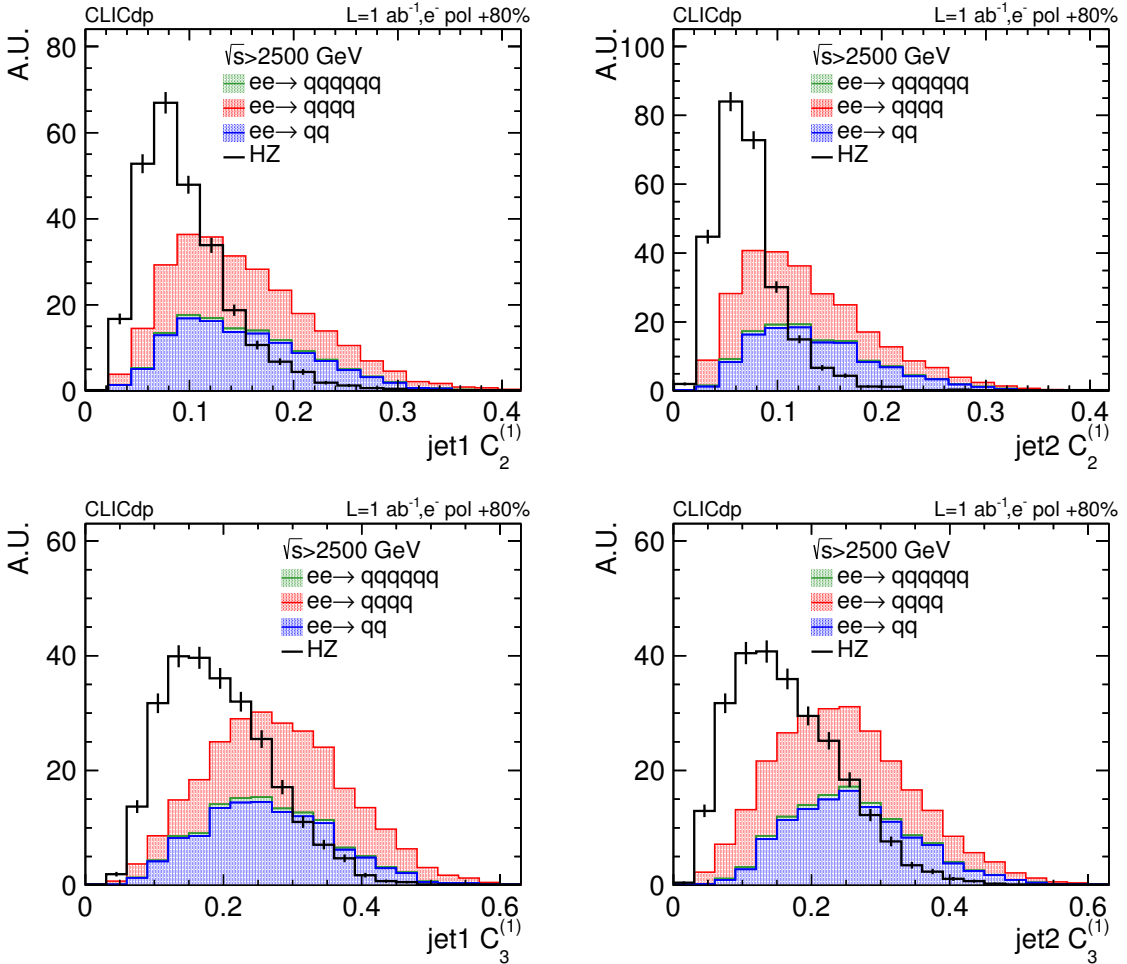


Figure 21: The jet energy correlation ratio distribution  $C_2^{(1)}$  (top) and  $C_3^{(1)}$  (bottom) for the leading (left) and sub-leading (right) jet for signal and background events with positive electron beam polarisation after the preselection on jet masses.

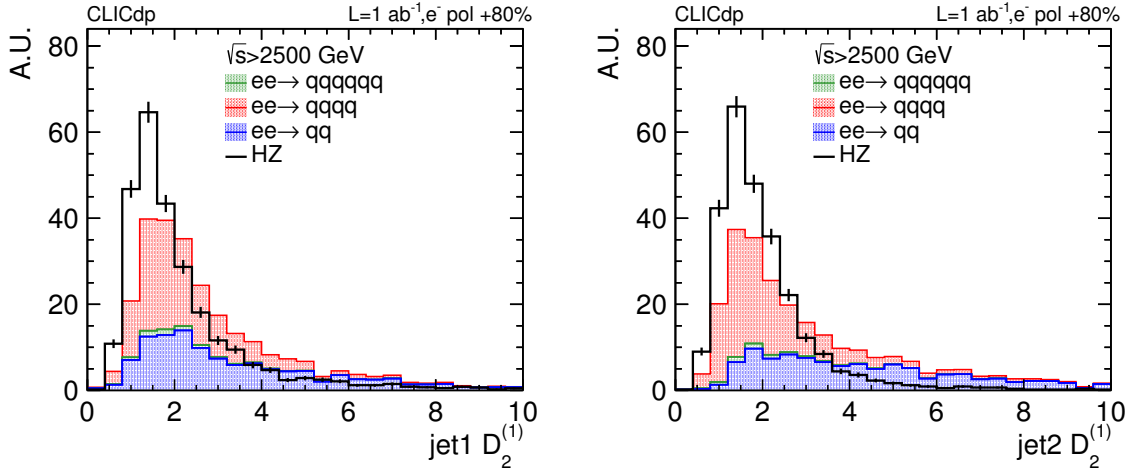


Figure 22: The jet energy correlation ratio  $D_2^{(1)}$  for the leading (left) and sub-leading jet (right) for signal and background events with positive electron beam polarisation after the preselection on jet masses.

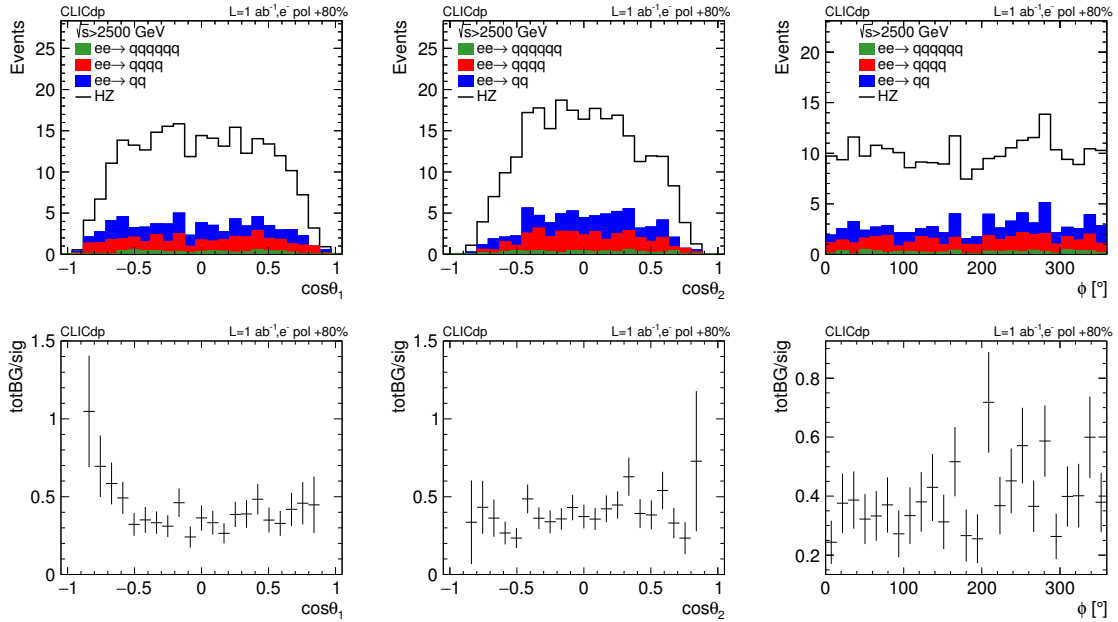


Figure 23: The three reconstructed angular distributions of  $\cos \theta_1$  (left),  $\cos \theta_2$  (centre), and  $\phi$  (right) for signal and background events with positive electron beam polarisation. The lower plots show the ratios between background and signal events after the preselection on jet masses.